THE JOURNAL OF BIOLOGICAL CHEMISTRY VOL. 291, NO. 45, pp. 23490–23505, November 4, 2016

Cardiac Ryanodine Receptor (Ryr2)-mediated Calcium Signals Specifically Promote Glucose Oxidation via Pyruvate Dehydrogenase*[S]

Received for publication, September 8, 2016 Published, JBC Papers in Press, September 12, 2016, DOI 10.1074/jbc.M116.756973

Michael J. Bround[‡§], Rich Wambolt[‡¶], Haoning Cen[‡§], Parisa Asghari[‡§], Razvan F. Albu[‖], Jun Han[‡‡], Donald McAfee[‡§§], Marc Pourrier[‡§§], Nichollas E. Scott[‖**], Lubos Bohunek[¶], Jerzy E. Kulpa[‖], S. R. Wayne Chen[¶¶], David Fedida[‡§§], Roger W. Brownsey[‖], Christoph H. Borchers[‡‡], Leonard J. Foster[‖**], Thibault Mayor[‖**], Edwin D. W. Moore[‡§], Michael F. Allard[‡¶], and James D. Johnson[‡§1]**

*From the [‡]Cardiovascular Research Group, Life Sciences Institute and Departments of [§]Cellular and Physiological Sciences, [‖]Biochemistry and Molecular Biology, and [§§]Anesthesiology, Pharmacology and Therapeutics, University of British Columbia, Vancouver, British Columbia V6T 1Z3, the [¶]Department of Pathology and Laboratory Medicine, University of British Columbia and the Centre for Heart and Lung Innovation, St. Paul's Hospital, Vancouver, British Columbia V6Z 1Y6, the **Michael Smith Laboratories, University of British Columbia, Vancouver, British Columbia V6T 1Z4, the [‡‡]University of Victoria-Genome British Columbia Proteomics Centre, Victoria, British Columbia V8Z 7X8, and the [¶¶]Libin Cardiovascular Institute of Alberta, Department of Physiology and Pharmacology, University of Calgary, Calgary, Alberta T2N 2T9, Canada*

Edited by Jeffrey Pessin

Cardiac ryanodine receptor (Ryr2) Ca^{2+} release channels and cellular metabolism are both disrupted in heart disease. Recently, we demonstrated that total loss of *Ryr2* leads to cardiomyocyte contractile dysfunction, arrhythmia, and reduced heart rate. Acute total Ryr2 ablation also impaired metabolism, but it was not clear whether this was a cause or consequence of heart failure. Previous *in vitro* studies revealed that Ca^{2+} flux into the mitochondria helps pace oxidative metabolism, but there is limited *in vivo* evidence supporting this concept. Here, we studied heart-specific, inducible *Ryr2* haploinsufficient (c*Ryr2*Δ50) mice with a stable 50% reduction in Ryr2 protein. This manipulation decreased the amplitude and frequency of cytosolic and mitochondrial Ca^{2+} signals in isolated cardiomyocytes, without changes in cardiomyocyte contraction. Remarkably, in the context of well preserved contractile function in perfused hearts, we observed decreased glucose oxidation, but not fat oxidation, with increased glycolysis. c*Ryr2*Δ50 hearts exhibited hyperphosphorylation and inhibition of pyruvate dehydrogenase, the key Ca^{2+}-sensitive gatekeeper to glucose oxidation. Metabolomic, proteomic, and transcriptomic analyses revealed additional functional networks associated with altered metabolism in this model. These results demonstrate that Ryr2 controls mitochondrial Ca^{2+} dynamics and plays a specific, critical role in promoting glucose oxidation in cardiomyocytes. Our findings indicate that partial RYR2 loss is sufficient to cause metabolic abnormalities seen in heart disease.

The type 2 ryanodine receptor (Ryr2)[2] sarcoplasmic reticulum (SR) Ca^{2+} release channel plays a central role in cardiac excitation-contraction coupling (1). Ca^{2+} signals generated by RYR2 have also been implicated in heart rate (2–5), hypertrophic gene regulation (6, 7), and cardiomyocyte superstructure (8, 9). Partially reduced Ryr2 expression, channel density, and/or signaling have been identified in models of aging (10) and heart disease (9, 11–13), which are conditions associated with metabolic dysfunction and a lack of energy substrate flexibility (14, 15). However, it remains to be determined whether a partial reduction in Ryr2 signaling can drive adult cardiac metabolic dysfunction.

SR Ca^{2+} release channels are known to transmit privileged Ca^{2+} signals into adjacent mitochondria (16). Based on *in vitro* studies, it has been proposed that these Ca^{2+} signals stimulate mitochondrial oxidative energy metabolism via pyruvate dehydrogenase (Pdh), key tricarboxylic acid (TCA) cycle enzymes, the electron transport chain, and the mitochondrial ATPase (17–19). These concepts have been extended to cardiac biology, where studies have shown a link between mitochondrial Ca^{2+} and energy production in the heart (20–27). However, direct *in vivo* evidence that Ca^{2+} flux from SR specifically paces mitochondrial oxidative glucose metabolism in normally function-

* This work was supported by University of British Columbia Start-Up Funds (to J. D. J.), funding from the Canadian Institutes of Health Research (CIHR) (MOP-77688) (to L. J. F.) and (MOP 115158) (to E. D. W. M.), a scholarship from CIHR (to M. J. B.), a scholarship from the Michael Smith Foundation for Health Research (to N. E. S.), and Natural Sciences and Engineering Research Council of Canada (NSERC) and the Heart and Stroke Foundation/Libin Cardiovascular Institute Professorship in Cardiovascular Research (to S. R. W. C.). The authors declare that they have no conflicts of interest with the contents of this article.

[S] This article contains supplemental Tables S1–S4, a supplemental Transcriptomics Data File, and a supplemental Proteomics Data File.

[1] To whom correspondence should be addressed: Life Sciences Institute, Dept. of Cellular and Physiological Sciences, University of British Columbia. 5358, 2350 Health Sciences Mall, Vancouver, British Columbia V6T 1Z3, Canada. Tel.: 604-822-7187; Fax: 604-822-2316; E-mail: james.d.johnson@ubc.ca.

[2] The abbreviations used are: Ryr2, ryanodine receptor type 2; Pdh, pyruvate dehydrogenase; Pdk, pyruvate dehydrogenase kinase; Pdp, pyruvate dehydrogenase phosphatase; SILAM, stable isotope labeling of amino acids in mice; SR, sarcoplasmic reticulum; TCA, tricarboxylic acid; AM, acetoxymethyester; UPLC-FTMS, ultra performance-Fourier transform mass spectrometry; UPLC-MRM/MS, ultra performance-liquid chromatography-multiple reaction monitoring-mass spectrometry; qPCR, quantitative RT-PCR; RU, relative units.

ing cardiomyocytes has not been published. We recently reported that complete *Ryr2* gene knock-out in adult mouse cardiomyocytes results in broad defects in energy metabolism (4, 20), but our previous model rapidly progressed to heart failure and sudden cardiac death (4), making it difficult to know whether mitochondrial metabolism is modulated by Ryr2 in normally functioning cardiomyocytes. Given this previous work and the association between Ryr2 dysfunction (9, 11–13) and oxidative metabolism in heart disease (14, 15), it was of interest to further explore links between Ryr2 and energy production using improved models.

To determine the potential links between Ryr2 and metabolism in the context of normal cardiac function, we devised a model where cardiomyocyte-specific, inducible Cre recombinase was used to delete only one *Ryr2* allele (c*Ryr2*Δ50 mice). Here, we report that a stable ~50% loss of Ryr2 protein in adult cardiomyocytes causes striking changes in mitochondrial Ca^{2+} cycling and is sufficient to specifically inhibit oxidative glucose metabolism but not fatty acid oxidation, lactate oxidation, or glycolysis. These metabolic effects occurred without significantly affecting cellular contraction or *in vivo* cardiac output, although we did observe a modest decrease in c*Ryr2*Δ50 heart rate. Our results suggest that pathophysiologically relevant loss of Ryr2 can account for the metabolic phenotype of failing hearts and that RYR2 plays a critical role in stimulating glucose oxidation *in vivo*.

Results

Previous studies have implicated the loss of RYR2 function or expression in disease states (9, 11–13). Similarly, analysis of publically accessible transcriptomic data on the National Center for Biotechnology Information Gene Expression Omnibus database (NCBI GEO) identified mouse and rat data sets with qualitatively reduced *Ryr2* mRNA (Fig. 1*A*).

To model partial *Ryr2* reduction, we deleted one *Ryr2* allele in adult mouse hearts. We confirmed ~50% ablation of *Ryr2* mRNA and protein in the c*Ryr2*Δ50 mice 3 weeks following the induction of haploinsufficiency with sequential tamoxifen injections (Fig. 1, *B–D*). Importantly, there was no compensation by other SR-Ca^{2+} release channel genes (Fig. 1*C*).

We examined the localization and organization of Ryr2 signaling structures using a Ryr2-GFP fusion protein knock-in allele (28). In c*Ryr2*Δ50 cardiomyocytes, Ryr2 puncta exhibited a grossly normal distribution, but were fewer, smaller, and less bright, with a more compact shape (Fig. 1*E*). Resolution past the diffraction limit of light will be required to further characterize the (dys)organization of these structures.

Confocal line-scanning microscopy and Ca^{2+} spark analysis revealed that c*Ryr2*Δ50 cardiomyocytes produced sparks with greater amplitude and slower kinetics than control cells (Fig. 1*F*). We did not observe a significant difference in spark frequency between the two groups (Fig. 1*G*), although we note that c*Ryr2*Δ50 cardiomyocytes may not follow a normal distribution and that the majority of c*Ryr2*Δ50 cells displayed lower spark frequency than the control average. These results suggest that there may be altered gating kinetics in c*Ryr2*Δ50 cardiomyocytes, but do not indicate gross alterations of channel open probabilities in a basal state.

To determine whether partial RYR2 ablation had an effect on SR Ca^{2+} load, we measured the size of caffeine-evoked Ca^{2+} responses in c*Ryr2*Δ50 cardiomyocytes (Fig. 1*H*). We did not observe a significant difference in caffeine-releasable Ca^{2+} between c*Ryr2*Δ50 and control cardiomyocytes.

We simultaneously measured cytosolic and mitochondrial Ca^{2+} in isolated cells stimulated with, in order, five single pulses of field stimulation, a period of continuous 0.5-Hz stimulation, and a period of 6-Hz pulses (Fig. 2). Both control and c*Ryr2*Δ50 cardiomyocytes responded to field stimulation and displayed similar Ca^{2+} dynamics to pulse or 0.5-Hz stimulation, revealing that the cells had similar viability and basal function (Fig. 2*A* (*i* and *ii*)). However, c*Ryr2*Δ50 cardiomyocytes had modestly decreased cytosolic and mitochondrial systolic Ca^{2+} amplitudes at these frequencies (Fig. 2*A* (*i* and *ii*)). At 6 Hz, chosen to approximate the rapid murine heart rate, c*Ryr2*Δ50 cardiomyocytes had significantly different cytosolic and mitochondrial Ca^{2+} dynamics (Fig. 2, *A* (*iii*), *C*, and *D*). Specifically, c*Ryr2*Δ50 cytosolic and mitochondrial Ca^{2+} transients had a significantly lower frequency and were temporally disassociated by ~10 s (Fig. 2, *A* (*iii*), *C*, and *E*). Co-staining with MitoTracker confirmed correct Rhod-2 loading (Fig. 2*F*). These data collectively indicate that ~50% Ryr2 ablation disrupts SR-to-mitochondria communication.

We next examined the function of c*Ryr2*Δ50 cardiomyocytes, *in vitro* and *in vivo*. We did not observe significant changes in diastolic length, fractional shortening, the time to 50% peak contraction, or the time to 50% relaxation (Fig. 3, *A–D*), indicating that contractile function in individual cells is normal. Cardiac function in isolated perfused working hearts revealed small decreases in cardiac output, rate pressure product, and cardiac work in c*Ryr2*Δ50 hearts (Fig. 3, *E–G*). However, these changes were modest when compared with the dramatic mechanical dysfunction observed in total *Ryr2* knock-out hearts (4, 20). Echocardiography failed to show any significant differences in heart function in c*Ryr2*Δ50 mice 3 or 20 weeks following tamoxifen (Fig. 3, *H–I*). We have previously demonstrated that complete *Ryr2* gene knock-out results in reduced heart rate and fatal arrhythmia (4, 20). In the present study, we found an intermediate level of bradycardia in c*Ryr2*Δ50 mice using subcutaneously implanted ECG telemetry in freely moving, unanesthetized mice (Fig. 3, *J* and *K*). These experiments suggest that a stable, ~50% reduction in RYR2 is compatible with well preserved function *in vivo* and *in vitro*, although a mild impairment can be identified in the *ex vivo* working heart system.

Having shown that c*Ryr2*Δ50 cardiomyocytes have preserved function, we assessed cardiac energy metabolism. Unlike the total *RyR2*KO hearts (4), there was no change in total ATP levels in c*Ryr2*Δ50 hearts (Fig. 4*A*), suggesting that they are not significantly energy-deprived. Perfused working c*Ryr2*Δ50 hearts were employed to assess utilization and oxidation of multiple energy substrates. Simultaneous measurements revealed a significant decrease in glucose oxidation and an increase in glycolysis (Fig. 4, *B* and *C*). Fatty acid oxidation and lactate oxidation were not altered in these c*Ryr2*Δ50 hearts (Fig. 4, *D* and *E*). A metabolomic survey of tricarboxylic acid cycle intermediates in c*Ryr2*Δ50 heart tissue displayed significant

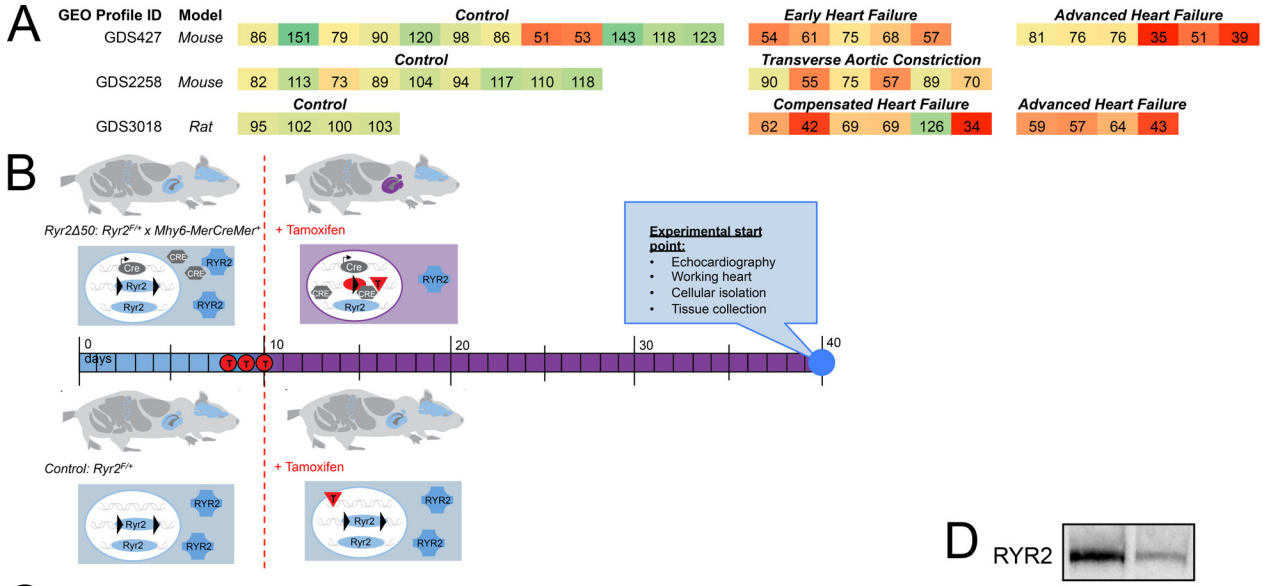
A
GEO Profile ID
Model
Control
Early Heart Failure
Advanced Heart Failure
GDS427 Mouse 86 151 79 90 120 98 86 51 53 143 118 123
54 61 75 68 57
81 76 76 35 51 39
Control
Transverse Aortic Constriction
GDS2258 Mouse 82 113 73 89 104 94 117 110 118
90 55 75 57 89 70
Control
Compensated Heart Failure
Advanced Heart Failure
GDS3018 Rat 95 102 100 103
62 42 69 69 126 34
59 57 64 43
B
Ryr2Δ50: Ryr2F/+ x Mhy6-MerCreMer+
+ Tamoxifen
Experimental start point:
Echocardiography
Working heart
Cellular isolation
Tissue collection
days
Control: Ryr2F/+
+ Tamoxifen

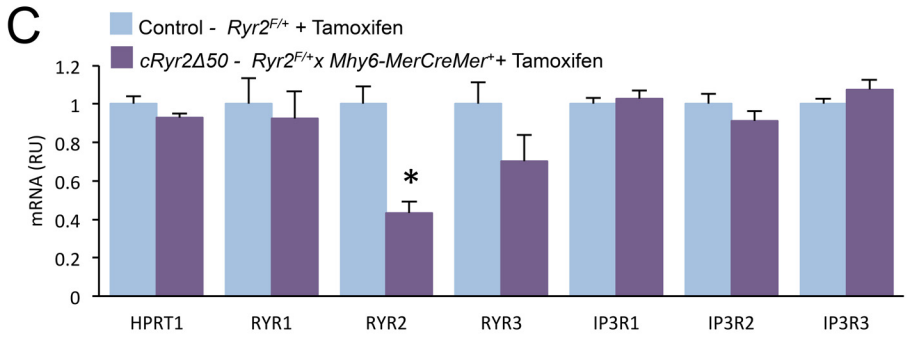
C
Control - Ryr2F/+ + Tamoxifen
cRyr2Δ50 - Ryr2F/+x Mhy6-MerCreMer+ + Tamoxifen
mRNA (RU)
HPRT1
RYR1
RYR2
RYR3
IP3R1
IP3R2
IP3R3

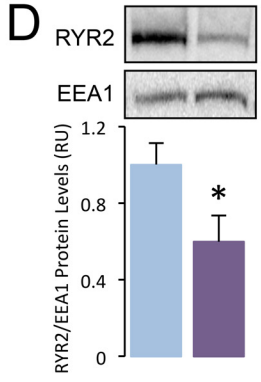
D
RYR2
EEA1
RYR2/EEA1 Protein Levels (RU)

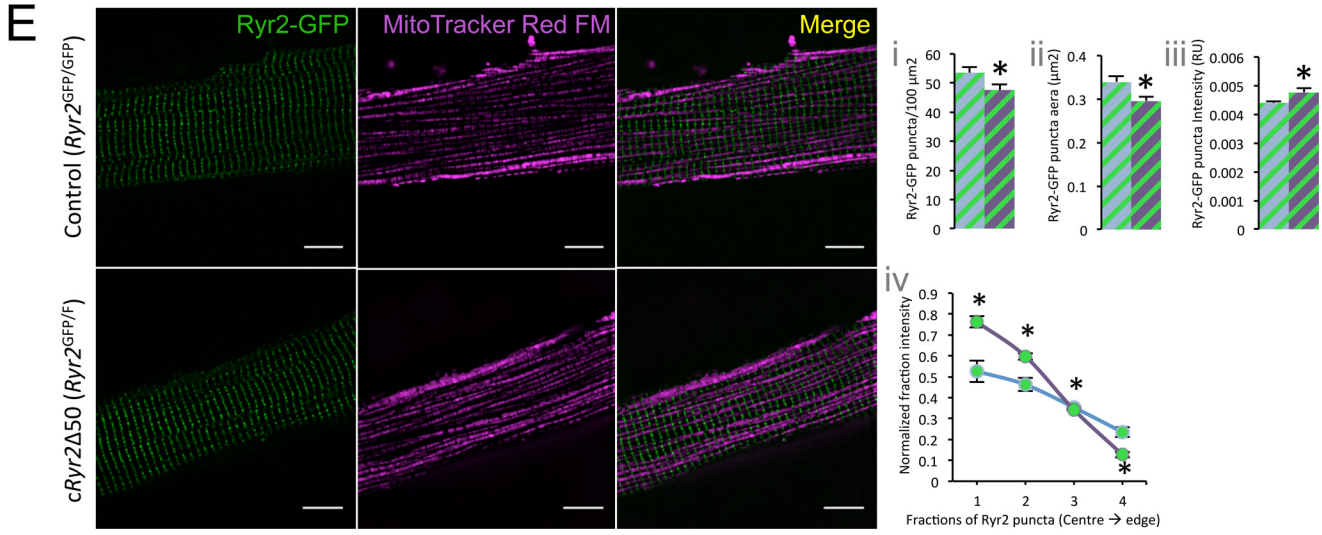
E
Ryr2-GFP
MitoTracker Red FM
Merge
Control (Ryr2GFP/GFP)
cRyr2Δ50 (Ryr2GFP/F)
i
Ryr2-GFP puncta/100 µm2
ii
Ryr2-GFP puncta aera (µm2)
iii
Ryr2-GFP puncta intensity (RU)
iv
Normalized fraction intensity
Fractions of Ryr2 puncta (Centre → edge)

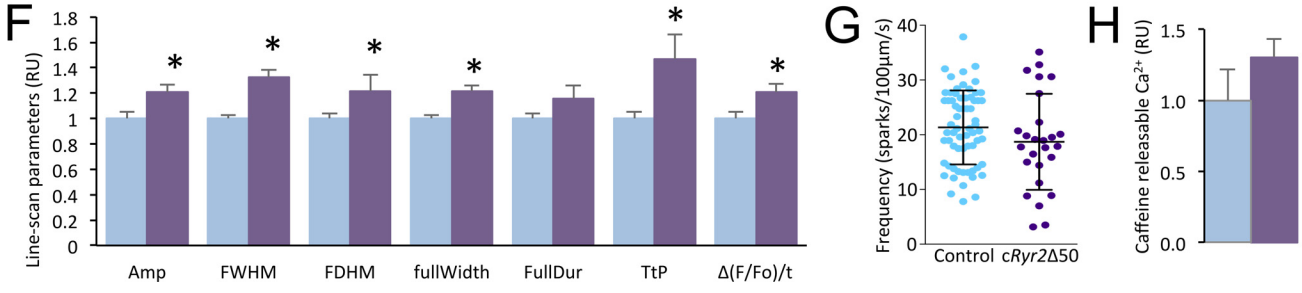
F
Line-scan parameters (RU)
Amp
FWHM
FDHM
fullWidth
FullDur
TtP
Δ(F/Fo)/t
G
Frequency (sparks/100µm/s)
Control
cRyr2Δ50
H
Caffeine releasable Ca2+ (RU)

decreases in fumarate and α-ketoglutarate, as well as a general trend toward decreased levels of other tricarboxylic acid cycle intermediates (Fig. 4*F*). Glycolytic metabolites upstream of entry into the tricarboxylic acid cycle, including pyruvate, remained unchanged in c*Ryr2*Δ50 hearts (Fig. 4*F*). These data demonstrate that glucose utilization is altered in c*Ryr2*Δ50 hearts in the absence of major cardiac dysfunction and suggest that Ryr2-mediated Ca^{2+} flux has a specific role in promoting the full oxidation of glucose in cardiac tissues *in vivo*.

To examine the molecular mechanism involved in this metabolic shift, we first focused on Pdh, the enzyme that catalyzes the conversion of pyruvate to acetyl-CoA. Pdh is a critical gatekeeper between glycolysis and complete glucose oxidation (29), and its activity is regulated by complex mechanisms involving inhibitory phosphorylation at three sites, including serine 293. Pdh phosphorylation is mediated by a family of Pdh kinases (*Pdk*1–4), whereas its dephosphorylation is catalyzed by a Ca^{2+}-sensitive phosphatase (Pdp1) (17). Initially, we found that Pdh phosphorylation was unchanged in the fed state (Fig. 4*G*). However, when we fasted mice overnight, c*Ryr2*Δ50 hearts displayed significantly increased Pdh phosphorylation levels (Fig. 4*H*). Consistent with this, fasted c*Ryr2*Δ50 hearts had significantly lower Pdh enzyme activity (Fig. 4*I*). There were no significant differences in *Pdk* expression between control and c*Ryr2*Δ50 hearts, although *Pdk4* was profoundly up-regulated following fasting in both groups (Fig. 4*J*). Together, our data demonstrate that, in the context of increased inhibitory Pdk tone during fasting, c*Ryr2*Δ50 mice are less efficient at dephosphorylating and reactivating Pdh activity than control mice. This is most likely explained by a decrease in the activity of Ca^{2+}-sensitive Pdp1 phosphatase caused by the reduced mitochondrial Ca^{2+} uptake downstream of Ryr2 ablation (Figs. 2 and 3*K*). We did not observe a difference in Akt phosphorylation between fasted c*Ryr2*Δ50 and control hearts (Fig. 4*L*), suggesting that insulin signaling through this pathway was normal under the conditions of our study.

To provide unbiased insight into the functional and metabolic effects of partial Ryr2 reduction, we performed proteomic analysis of extracts from fed-state control and c*Ryr2*Δ50 hearts, spiked with known amounts of SILAM wild type heart tissue (heavy labeled) to allow quantitative comparisons (Fig. 5*A*) (30). We identified 1702 unique proteins with high confidence after excluding blood-borne contaminants, and then compared their relative enrichment levels using the reference SILAM sample (Fig. 5*B*; supplemental Transcriptomics Data File). Most quantified proteins were similarly enriched with a few exceptions. The 35 most highly increased proteins included: Sacm1l, a regulator of inositol 1,4,5-trisphosphate (IP_3) signaling; Bmp10, a key regulator of heart development; atrial natriuretic factor, a cardio-protective hormone and biomarker of cardiac dysfunction (31); and Ahnak2, a large t-tubule protein that interacts with Ryr2 (32) (Fig. 5*B*). On the other hand, the 35 most highly decreased proteins included: Homer, which interacts with Ryr2 to decrease its open probability (33); and Ryr2 itself. Network analysis identified clusters of interacting proteins involved in heart muscle contraction, actin binding/motility, and muscle cell differentiation that were increased (Fig. 5*C*), as well as clusters of proteins involved in fatty acid oxidation/metabolism, mitochondrial inner membranes/matrix, contractile fibers, and TCA cycle that were enriched in the c*Ryr2*Δ50 heart proteome (Fig. 5*D*). This unbiased survey illustrates that hearts undergo metabolic and contractile remodeling as a result of partial Ryr2 deletion.

We mined our proteomic data to assess the status of c*Ryr2*Δ50 cardiomyocyte sarcomeres and mitochondria (Figs. 6 and 7). This targeted survey of core excitation-contraction proteins identified a modest decrease in the Na/Ca^{2+} exchanger Ncx1 (Fig. 6*A*). We also observed modest decreases in the troponin/tropomyosin complex and a large increase in atrial isoforms of regulatory and essential myosin light chains, which have been associated with heart disease (34), as well as increased levels of calponins, proteins that interact with actin and tropomyosin, which, when overexpressed, can partially rescue hearts from dilated cardiomyopathy (35). A survey of the glycolytic and glucose oxidation pathways showed no changes in core pathway enzymes (Fig. 6*B*). Instead, we observed reductions only in fructose-1,6-bisphosphatase 2 (Fbp2), an anabolic protein that counteracts the activity of phosphofructokinase 1 (Pfk1), the key gatekeeper of glycolysis (36), as well as Pdk1 and Pdk4, inhibitory kinases of the Pdh glucose oxidation gatekeeper (29) (Fig. 6*B*). These data suggest a reduction of inhibitory signals to both glycolysis and glucose oxidation in c*Ryr2*Δ50 hearts despite the reduced glucose oxidation and context-dependent Pdh hyperphosphorylation. A similar survey of the fat oxidation pathway shows modest decreases in the carnitine acyl-carnitine transporter and some β-oxidation proteins (Fig. 6*C*). However, because these changes failed to result in reduced palmitate oxidation rates, these changes must be within the range of dynamic regulation. We also observed a large decrease in NAD kinase and a large increase in nicotinamide *N*-methyltransferase (NNT), changes that are consistent with the cell trying to preserve reducing equivalents for the TCA cycle but that may also compromise the antioxidant capacity of the cell (37) (Fig. 6*C*). We did not observe robust changes in the electron transport chain or ATP synthase machinery sub-proteomes (Fig. 7). Collectively, this proteomic

FIGURE 1. **Generation of an inducible, heart-specific, partial Ryr2 ablation model (*Ryr2*Δ*50*).** *A*, selected *Ryr2* transcriptomics data from NCBI GEO were re-normalized to the average of their control values and presented as a heat map. *B*, breeding scheme, experimental design, and analysis timeline. *C*, c*Ryr2*Δ50 cardiomyocytes have a specific reduction in Ryr2 mRNA, and no compensation from other known endoplasmic reticulum (ER)/SR Ca^{2+} channels ($n = 4–8$, *, $p \leq 0.05$). *Blue bars* = control ($Ryr2^{flox/wildtype}$ + tamoxifen), *purple bars* = c*Ryr2k*Δ50 ($Ryr2^{flox/wildtype} \times Mhy6\text{-}MerCreMer^{+}$ + tamoxifen) throughout. *D*, cardiac RYR2 protein levels in c*Ryr2*Δ50 mice 3 weeks after tamoxifen ($n = 7$, *, $p \leq 0.05$). *E*, images of Ryr2-GFP fusion proteins in isolated cardiomyocytes from control ($Ryr2^{GFP/GFP}$) and c*Ryr2*Δ50 ($Ryr2^{GFP/flox} \times$ Mhy6-MerCreMer + tamoxifen) mice ($n = 9$ cells/group; *scale bar*, 10 μm). Images were quantified for Ryr2-GFP puncta number (*panel i*), area (*panel ii*), and intensity (*panel iii*). A measure of puncta intensity distribution (mean fractional brightness from the center to the edge of the puncta) was also quantified (*panel iv*). *, $p \leq 0.05$. *F*, line-scanning spark measurement parameters of c*Ryr2*Δ50 cardiomyocytes (control $n = 70$, c*Ryr2*Δ50 $n = 26$; data from three cell isolations, *, $p \leq 0.05$) *Amp*, amplitude; *FWHM*, full width at half maximum; *FDHM*, full duration at half maximum; *fullWidth*, full width; *FullDur*, full duration; *TtP*, time to peak. *G*, spark frequency in isolated c*Ryr2*Δ50 cardiomyocytes (control $n = 70$, c*Ryr2*Δ50 $n = 26$; data from three cell isolations). *H*, peak Fluo-4 intensity following 3 mM caffeine treatment of control ($n = 5$) and *cRyr2*Δ50 cardiomyocytes ($n = 6$). All data were plotted as mean ± S.E.

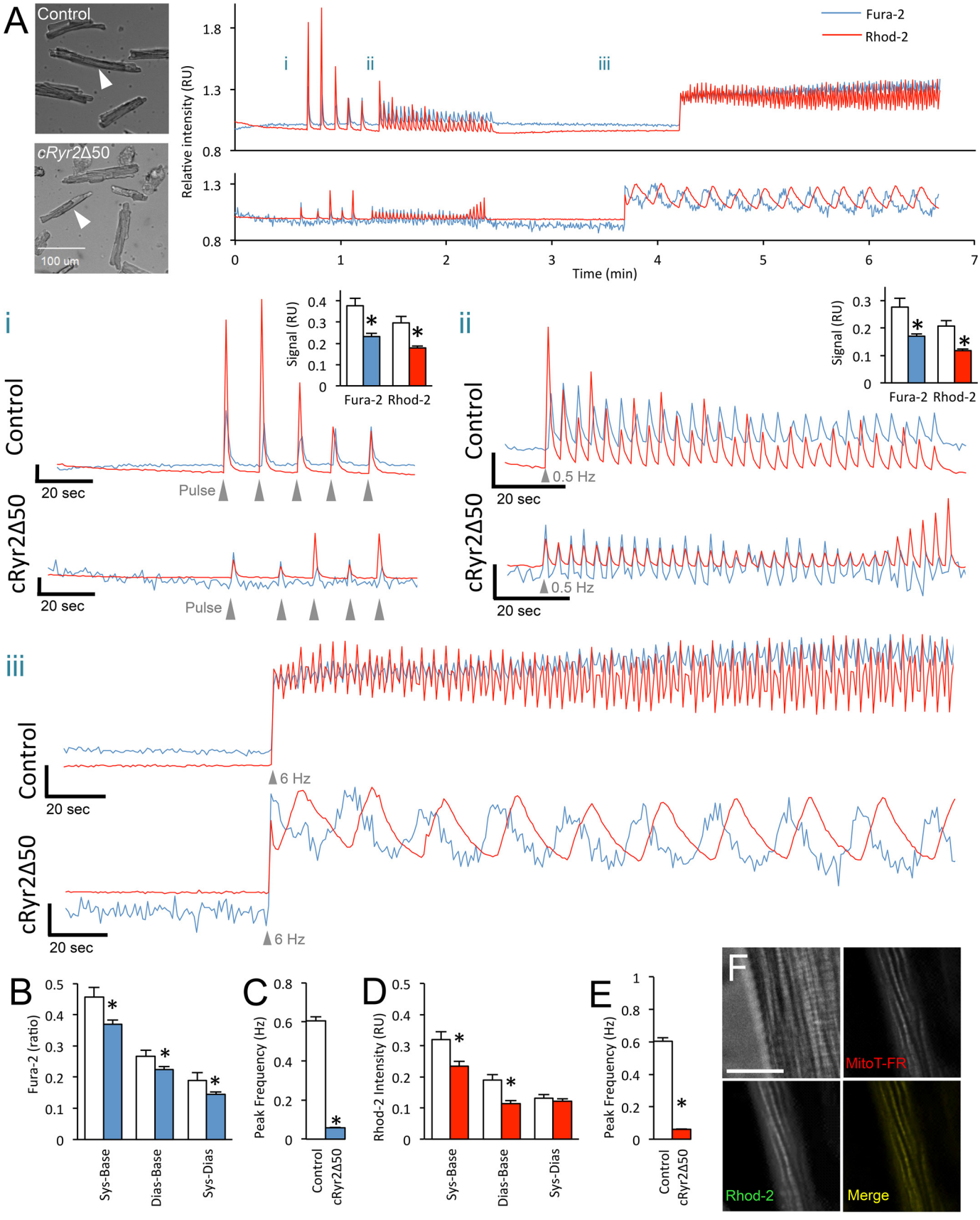
A
Control
cRyr2Δ50
100 um
Fura-2
Rhod-2
Relative intensity (RU)
Time (min)
i
ii
iii
Signal (RU)
Fura-2 Rhod-2
Control
cRyr2Δ50
20 sec
Pulse
0.5 Hz
6 Hz
B
Fura-2 (ratio)
Sys-Base
Dias-Base
Sys-Dias
C
Peak Frequency (Hz)
Control
cRyr2Δ50
D
Rhod-2 Intensity (RU)
E
F
MitoT-FR
Rhod-2
Merge

analysis revealed changes initiated by the stable 50% reduction in Ryr2 that are likely to contribute to effects on metabolism.

Our mass spectrometry-based proteomic analysis was not able to assess every gene product. Thus, RNA sequencing was also employed to provide genome-wide analysis of changes in fed-state c*Ryr2*Δ50 hearts. There were relatively few changes in the transcriptome of c*Ryr2*Δ50 hearts that reached genome-wide significance (Fig. 8*A*; supplemental Proteomics Data File). However, notable differences included decreased expression of *Ryr2* (Fig. 8*B*), voltage-gated Na^+ channel *Scn4b* (Fig. 8*C*), and *Mylk4* (Fig. 8*D*), a novel isoform of myosin light chain kinase that is down-regulated in heart failure (38). We also found decreased expression of *Ucp1* and *Cbr2* genes that utilize TCA reducing equivalents for non-energy-producing processes but potentially at the expense of protection from reactive oxygen species (39) (Fig. 8*E*). Biosynthetic genes were also significantly decreased in c*Ryr2*Δ50 hearts, including key gluconeogenesis gene *Pck1* and *Gpd1*, a protein that scavenges glycolysis products for sugar biosynthesis (Fig. 8*F*). *Cbr2* and *Gpd1* were also observed to be decreased in the heart proteome (Figs. 6*C* and 7). We also observed a general up-regulation of extracellular structural and remodeling genes consistent with cardiac pathology (40) (Fig. 8*G*). In summary, the c*Ryr2*Δ50 heart transcriptome also revealed contractile and metabolic modulation/compensation.

Discussion

The goal of the present study was to examine the effects of ~50% reduction in Ryr2 on heart metabolism and function. We found that a stable 50% loss of Ryr2 protein impaired mitochondrial Ca^{2+} signaling, reduced Ca^{2+}-dependent Pdh activation, and specifically reduced oxidative glucose metabolism. Importantly, these changes occurred in the absence of robust mechanical dysfunction, meaning that they are primary effects downstream of Ryr2. Unbiased proteomic and transcriptomic surveys of c*Ryr2*Δ50 hearts revealed alterations in contractile and metabolic gene networks predicted to increase glucose oxidation and Ryr2 Ca^{2+} release, suggesting mechanisms for compensation in this model.

Our principle finding is that Ryr2 specifically promotes glucose oxidation in cardiomyocytes. A wealth of *in vitro* research has shown that mitochondrial Ca^{2+} signaling is important for the oxidation of energy fuel substrates by stimulating TCA cycle enzymes, the electron transport chain, and ATP synthase (17–19). It had been previously proposed that glucose oxidation is controlled by Ca^{2+} signaling via the key gatekeeper for pyruvate entry into the TCA cycle, Pdh, which is activated by a Ca^{2+}-sensitive phosphatase (Pdp) (17, 29). To the best of our knowledge, our work is the first *in vivo* demonstration of an ionic mechanism that specifically controls glucose oxidation, but not fat oxidation. The finding that Ryr2-to-mitochondria Ca^{2+} signals play a specific and sensitive role in promoting glucose oxidation may represent a key mechanism by which the metabolic demands of excitation-contraction are directly coupled to the rate of ATP production in cardiomyocytes.

Glucose oxidation contributes to cardiomyocyte energy metabolism and is preferentially up-regulated in periods of oxidative stress or increased metabolic demand (14). It is notable that we only observed the effects of Ryr2 haploinsufficiency on Pdh phosphorylation/activity in fasted c*Ryr2*Δ50 mice. Fasting increased *Pdk4* expression, which would be expected to increase the inhibitory phosphorylation tone on the Pdh system (41). In this metabolic stress situation, the phosphatase activity of Pdp may be more important for reactivating Pdh to allow for effective glucose oxidation (42). Our findings suggest that, in this context, Ryr2 becomes necessary to fully drive Pdp activity and prevent hyperphosphorylation of Pdh. The effects of Ryr2 on Pdh activation may have been partially obscured by basal reductions in Pdk1 and Pdk4 in the fed-state c*Ryr2*Δ50 heart proteome, suggesting the possibility that Pdh activation may normally be even more sensitive to Ryr2 than our experiments revealed. Nevertheless, our data clearly demonstrate, for the first time, that Ryr2 is critically involved in preferentially increasing glucose oxidation during metabolic stress. The fasting dependence of this system is reminiscent of the conditions required to uncover changes in Pdh regulation in mice lacking the mitochondrial Ca^{2+} uniporter, which required either a metabolic or β-adrenergic stress to display altered Pdh regulation (23, 25).

Our previous research measured the effects of total Ryr2 deletion on oxidative metabolism and reported reduced heart ATP levels and a general reduction in total oxidative energy metabolism (20). The present study demonstrates that a 50% Ryr2 reduction specifically disrupts glucose oxidation, which suggests that there may be a hierarchy where oxidative metabolism of multiple substrates is generally Ca^{2+}-sensitive, but glucose oxidation is attuned to more subtle changes in mitochondrial Ca^{2+}. Because glucose oxidation and glycolysis are frequently uncoupled in models of heart disease before the general impairment of oxidative metabolism seen in heart failure (14, 15), these data also suggest that progressive Ryr2 dysfunc-

FIGURE 2. **Cytosolic and mitochondrial Ca^{2+} in c*Ryr2*Δ50 cardiomyocytes.** *A*, representative simultaneous Fura-2 and Rhod-2 fluorescence traces from healthy control and *cRyr2*Δ50 cardiomyocytes. Bright field images with *arrows* indicate individual cardiomyocytes from which traces are derived. *Panel i*, enlargement of pulse stimulation region. Scale axis begins at 0.9 RU. *Inset graphs* show average peak systolic Fura-2 ratio and Rhod-2 intensity relative to baseline. *Panel ii*, enlargement of 0.5-Hz stimulation region. Scale axis begins at 0.9 RU. *Inset graphs* show average peak systolic Fura-2 ratio and Rhod-2 intensity relative to baseline. *Panel iii*, enlargement of 6-Hz stimulation region. Scale axis begins at 8.5 RU. *, $p \leq 0.05$. *B*, average Fura-2 ratio in control and *cRyr2*Δ50 cardiomyocytes during 6-Hz stimulation. *White bars* = control; *solid color bars* = *cRyr2*Δ50 throughout (mean ± S.E.). *Sys-Base* denotes the difference between average peak systolic and baseline measurements, *Dias-Base* denotes the difference between average minimal diastolic and average baseline measurements, and *Sys-Dias* denotes the difference between peak systolic and minimum diastolic measurements. *, $p \leq 0.05$. *C*, average frequency of cytosolic Ca^{2+} transients elicited during 6-Hz stimulation. *, $p \leq 0.05$. *D*, average Rhod-2 intensity in control and *cRyr2*Δ50 cardiomyocytes during 6-Hz stimulation. *, $p \leq 0.05$. *E*, average frequency of elicited mitochondrial Ca^{2+} transients observed during 6-Hz stimulation. For all average values: control $n = 63$ cells, c*Ryr2*Δ50 $n = 141$ cells, three independent cell preparations from three mice per treatment; *, $p \leq 0.05$. *F*, high resolution microscopy of isolated mouse cardiomyocyte showing colocalization of Rhod-2-AM and MitoTracker Deep Red dye (MitoT-FR). Fluorescent channel images are from a single optical plane from a deconvolved wide field z-stack. *Scale bar* is 10 μm. All data were plotted as mean ± S.E. Control = $Ryr2^{flox/wildtype}$ + tamoxifen; *cRyr2*Δ50 = $Ryr2^{flox/wildtype}$ × *Mhy6*-MerCreMer$^+$ + tamoxifen.

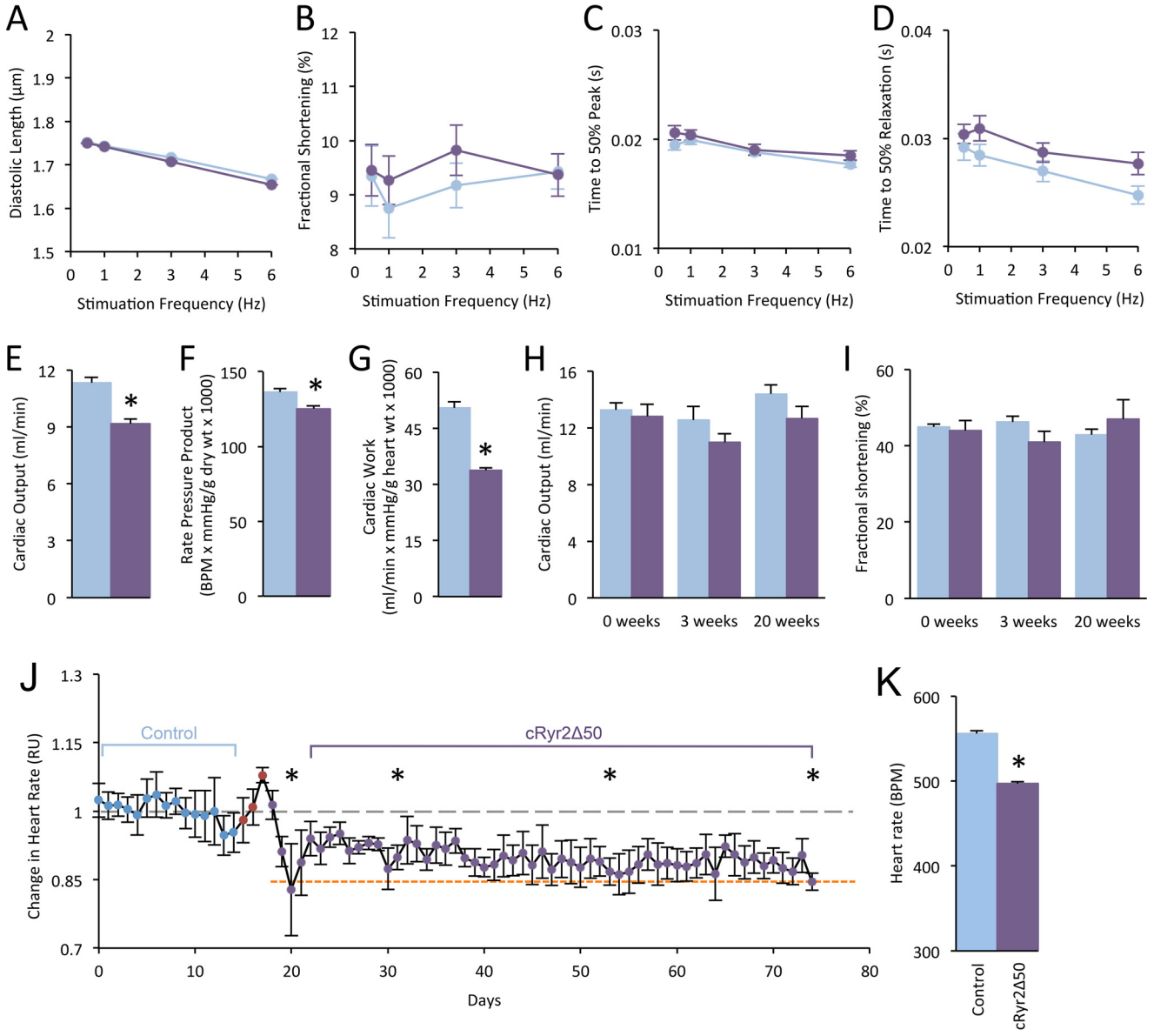

FIGURE 3. **Cardiac function and heart rate in *cRyr2*Δ50 mice.** *A* and *B*, isolated cardiomyocytes were assessed for average diastolic length (*A*) and fractional shortening (*B*) upon stimulation ($n = 3$; *, $p \leq 0.05$.). *C* and *D*, isolated cardiomyocyte contraction rate reported as time to 50% peak contraction (*C*) and time to 50% peak relaxation (*D*). *White circles* = control; *black circles* = *cRyr2*Δ50. *E–G*, cardiac output (*E*), rate pressure product (*F*), and cardiac work (*G*) measured during working heart perfusions (control $n = 10$, *cRyr2*Δ50 $n = 13$; *, $p \leq 0.05$.). *White bars* = control; *black bars* = *cRyr2*Δ50; throughout. Echocardiograms of control and *cRyr2*Δ50 mice 3 weeks following tamoxifen treatment are shown. *BPM*, beats per minute. *H* and *I*, average cardiac output (*H*) and fractional shortening (*I*) of control and *cRyr2*Δ50 mice 3 and 20 weeks following tamoxifen treatment ($n = 5$). *J*, average heart rate from implantable ECG radio telemetry. *Blue points* denote days prior to tamoxifen injections (*red points*), but following surgical recovery and the removal of analgesics. Heart rate is normalized to the average heart rate measured during baseline (*gray dashed line*). The *red dashed line* denotes average heart rate of the total cRyr2KO mice reported in our previous publication (4) *K*, average heart rate before and after tamoxifen treatment (mean ± S.E.; $n = 5$; *, $p \leq 0.05$). All data were plotted as mean ± S.E. Control = $Ryr2^{flox/wildtype}$ + tamoxifen; *cRyr2*Δ*50:* $Ryr2^{flox/wildtype} \times Mhy6\text{-}MerCreMer^{+}$ + tamoxifen.

tion in disease may contribute to mounting metabolic dysfunction in a "dose-dependent" manner.

Our results indicate that a 50% reduction in Ryr2 changes the frequency and amplitude of cytosolic and mitochondrial Ca^{2+} signals. Because groups of Ryr2 normally function in concert, due to proximity and physical interaction (8), it is possible that decreasing Ryr2 abundance reduced the functional coupling within the Ryr2 signaling apparatus, leading to more gradual activation and deactivation of Ca^{2+} transients. Our data also suggest disrupted privileged communication between Ryr2 and mitochondria. Mitochondria rely on microdomain signaling where the mitochondrial Ca^{2+} uniporter is paired with Ca^{2+} release channels to drive mitochondrial Ca^{2+} uptake (16). Our data suggest that when Ryr2 is reduced, Ca^{2+} cannot flow as quickly between these two organelles via microdomain signaling. It is possible that deleting 50% of Ryr2 proteins disrupts SR-mitochondria tethering (43, 44). Ultra-structural/super-resolution analysis of Ryr2 in this mouse model could form the basis of a future study.

Another important finding of this study is that a 50% decrease in Ryr2 is sufficient to significantly reduce heart rate. In our previous work on total *cRyr2* knock-out mice, we noted

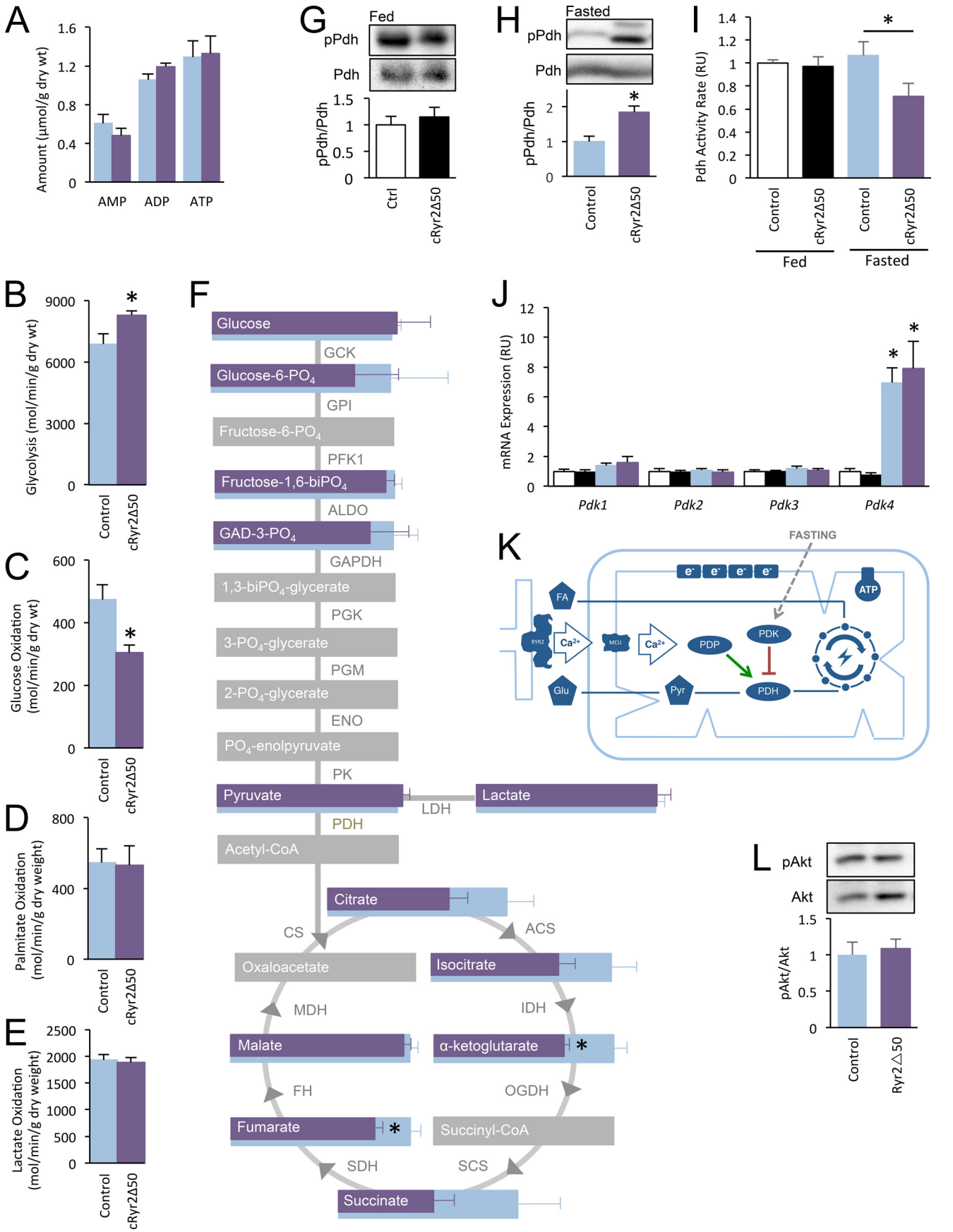
A
Amount (µmol/g dry wt)
1.6
1.2
0.8
0.4
0
AMP
ADP
ATP
G
Fed
pPdh
Pdh
pPdh/Pdh
1.5
1
0.5
0
Ctrl
cRyr2Δ50
H
Fasted
pPdh
Pdh
pPdh/Pdh
2
1
0
*
Control
cRyr2Δ50
I
Pdh Activity Rate (RU)
1.4
1.2
1
0.8
0.6
0.4
0.2
0
*
Control
cRyr2Δ50
Control
cRyr2Δ50
Fed
Fasted
B
Glycolysis (mol/min/g dry wt)
9000
6000
3000
0
*
Control
cRyr2Δ50
C
Glucose Oxidation (mol/min/g dry wt)
600
400
200
0
*
Control
cRyr2Δ50
D
Palmitate Oxidation (mol/min/g dry weight)
800
400
0
Control
cRyr2Δ50
E
Lactate Oxidation (mol/min/g dry weight)
2500
2000
1500
1000
500
0
Control
cRyr2Δ50
F
Glucose
GCK
Glucose-6-PO4
GPI
Fructose-6-PO4
PFK1
Fructose-1,6-biPO4
ALDO
GAD-3-PO4
GAPDH
1,3-biPO4-glycerate
PGK
3-PO4-glycerate
PGM
2-PO4-glycerate
ENO
PO4-enolpyruvate
PK
Pyruvate
LDH
Lactate
PDH
Acetyl-CoA
Citrate
CS
ACS
Oxaloacetate
Isocitrate
MDH
IDH
Malate
α-ketoglutarate
*
FH
OGDH
Fumarate
*
Succinyl-CoA
SDH
SCS
Succinate
J
mRNA Expression (RU)
12
10
8
6
4
2
0
*
*
Pdk1
Pdk2
Pdk3
Pdk4
K
FASTING
e-
e-
e-
e-
ATP
FA
RYR2
Ca2+
MCU
Ca2+
PDP
PDK
Glu
Pyr
PDH
L
pAkt
Akt
pAkt/Akt
1.5
1
0.5
0
Control
Ryr2△50

a substantial reduction in heart rate, as well as tachycardic arrhythmias (4). Our results here show that even in the absence of acute mechanical dysfunction, stable *Ryr2* haploinsufficiency is sufficient to reduce heart rate, which provides evidence that this is a *bona fide* effect of Ryr2 signaling and not a consequence of heart dysfunction (4). This provides further strong evidence that Ryr2 is critical for cardiac pace-making and supports a model where heart rate is regulated by an ensemble of SR and plasma membrane ion channels (2).

The c*Ryr2*Δ50 mouse line is a major improvement on previous loss-of-function Ryr2 models as it is not lethal and does not show the dramatic changes in cardiac mechanical function found in total c*Ryr2*KO mice (heart-specific, inducible *Ryr2* gene knockout mice). Our c*Ryr2*Δ50 model also greatly reduces the potential for confounding long-term compensatory effects of global, life-long mutations (7), as well as the putative period of tamoxifen drug effects observed in some studies (45). Additionally, induced Ryr2 haploinsufficiency models a situation analogous to disease conditions with a decrease in either Ryr2 expression or function (9–13) (Fig. 1*A*). Indeed, numerous studies have reported reduced Ryr2 levels or function in diabetic cardiomyopathy (11), heart failure (12, 13), and aging (10), implicating Ryr2 dysfunction as an element of heart disease and its predisposing conditions. Heart disease is also associated with reductions in the oxidative capacity of the heart and reductions in the metabolic flexibility including reduced glucose oxidation and increased glycolysis (4). Our study shows that a chronic 50% reduction of Ryr2 in adult animals, similar to what is seen in multiple disease states, is sufficient to disrupt normal glucose oxidation in cardiomyocytes. Thus, Ryr2 dysfunction may contribute to the impaired metabolic flexibility seen in heart disease.

Materials and Methods

Experimental Animals—All animal protocols were approved by the University of British Columbia Animal Care Committee in accordance with international guidelines. Mice with "floxed" Ryr2 alleles were generated and characterized previously (4, 5, 20). Tamoxifen-inducible, cardiomyocyte-specific Ryr2 haploinsufficiency mice (*cRyr2*Δ50 mice) were generated by crossing C57Bl6 $Ryr2^{flox/wildtype}$ mice with C57Bl6 *mer-cre-mer*; strain: 005657, The Jackson Laboratory, Bar Harbor, ME). Tamoxifen was injected i.p. into 8–16-week-old $Ryr2^{flox/wildtype}$:*mer-Cre-mer* mice and littermate control mice ($Ryr2^{flox/wildtype}$ mice injected with tamoxifen) for 3 consecutive days at 3 mg/40 g of body weight. All mice were given >3 weeks recovery after tamoxifen to reach stable Ryr2 ablation and to circumvent any possible effects of tamoxifen, which is cleared from mice within 21 days (Fig. 1*B*) (45).

Ryr2 puncta quantification employed a Ryr2-GFP fusion protein knock-in allele (28). Cre-expressing, tamoxifen injected $Ryr2^{flox/GFP}$ mice were compared with tamoxifen-injected $Ryr2^{GFP/GFP}$ littermate controls.

C56Bl6 SILAM mice (30) were generated by feeding mice MouseExpress L-LYSINE ($^{13}C6$, 99%) at 8 g/kg of diet (Cambridge Isotope Laboratories, Andover, MA) for two generations. Amino acid incorporation within long-lived neuronal tissue was confirmed to be >97%.

To assess differences in Pdh activity, some mice were fasted for 16 h. All other data were collected from *ad libitum* fed mice with a rodent chow diet.

Imaging and Functional Measurements—All live cell analysis was conducted on cardiomyocytes isolated from *cRyr2*Δ50 and control mice using Langendorff reverse perfusion to introduce collagenase to the cardiac vasculature (46). All live cardiomyocyte analysis occurred within 8 h of cell isolation, and only rod-shaped cardiomyocytes with typical cell morphology were considered in analysis.

Ryr2-GFP puncta were imaged in cardiomyocytes counterstained with 5 μM MitoTracker Red FM (Thermo Fisher) for 15 min, followed by a 5-min wash, using a 100×/1.45 oil objective on a spinning disk confocal system based on Zeiss Axiovert 200M microscope. 3D image stacks, acquired with identical settings, were deblurred by the Nearest Neighbor Deconvolution module of the SlideBook 6 software (Intelligent Imaging Innovations, Denver, CO), and five representative planes evenly distributed within each cell were selected for further quantifications using the CellProfiler software (Broad Institute). Unprocessed images were used for the analysis related to the fluorescence intensity of the identified Ryr2-GFP puncta.

Cardiomyocyte Ca^{2+} sparks of isolated cells loaded with 5 μM Fluo-4-AM were imaged through the 63× objective of a Zeiss LSM 700 confocal microscope in line scan mode (1053 lines per second, 0.142-μm pixel size) in minimal media. Sparks were quantified using SparkMaster, an ImageJ plugin (47).

To measure whole-cell Ca^{2+} signals, we employed a ratiometric Ca^{2+}-sensitive fluorescent dye, Fura-2-acetoxymethyester (AM) (Invitrogen). Mitochondrial Rhod-2-AM (Invitrogen) localization was confirmed by co-loading cardiomyocytes with 5 μM MitoTracker Deep Red (644/655 nm) (Invitrogen) and imaging at high resolution using a 100 × 1.45 NA objective on a Zeiss Axiovert-200M microscope with a CoolSnapHQ2 CCD Camera (Intelligent Imaging Innovations).

FIGURE 4. ***cRyr2*Δ50 mice have a specific defect in glucose oxidation, associated with hyperphosphorylation and reduced activity of Pdh.** *A*, average heart ATP, ADP, and AMP as measured by HPLC-chromatography on whole homogenized hearts ($n = 3$). *B* and *C*, non-oxidative glycolysis (*B*) and complete glucose oxidation (*C*) were simultaneously measured in working hearts (control $n = 5$, *cRyr2*Δ50 $n = 6$; *, $p \leq 0.05$). *Light blue bars* = control, *purple bars* = *cRyr2*Δ50 throughout. *D* and *E*, at the same time, palmitate oxidation (*D*) and lactate oxidation (*E*) were measured (control $n = 5$, c*Ryr2*Δ50 $n = 7$). *F*, diagram showing the results of targeted mass spectroscopy-based metabolomic analysis of TCA cycle acid intermediaries and glycolysis pathway sugar intermediates ($n = 8$; *, $p \leq 0.05$; *gray* = unmeasured). *GCK*, germinal center kinase; *GPI*, glycosylphosphatidylinositol; *PFK1*, phosphofructokinase 1; *ALDO*, aldo-keto reductase; *PGK*, phosphoglycerate kinase; *PGM*, phosphoglycerate mutase; *ENO*, eno/pyruvate carboxylase; PK, protein kinase. *G* and *H*, pyruvate dehydrogenase kinase E1-α subunit serine 293 phosphorylation levels in mice fed *ad libitum* (*white*, control $n = 3$; *black*, *cRyr2*Δ50 $n = 3$; *, $p \leq 0.05$) and fasted overnight (*blue*, control $n = 5$; *purple*, c*Ryr2*Δ50 $= 6$; *, $p \leq 0.05$). pPdh, phospho-Pdh; *Ctrl*, control. *I*, pyruvate dehydrogenase activity in *ad libitum* fed and overnight fasted whole homogenized hearts (fed control $n = 7$, fed c*Ryr2*Δ50 $n = 8$, fasted control $n = 8$, fasted *cRyr2*Δ50 $n = 8$; *, $p \leq 0.05$). *J*, pyruvate dehydrogenase kinase isoform mRNA levels in *ad libitum* fed and fasted c*Ryr2*Δ50 hearts ($n = 6$, *, $p \leq 0.05$). *K*, working model of context-dependent regulation of PDH activity by mitochondrial Ca^{2+}. *L*, assessment of Akt phosphorylation levels in overnight fasted c*Ryr2*Δ50 hearts ($n = 6$; *, $p \leq 0.05$). All data were plotted as mean ± S.E.

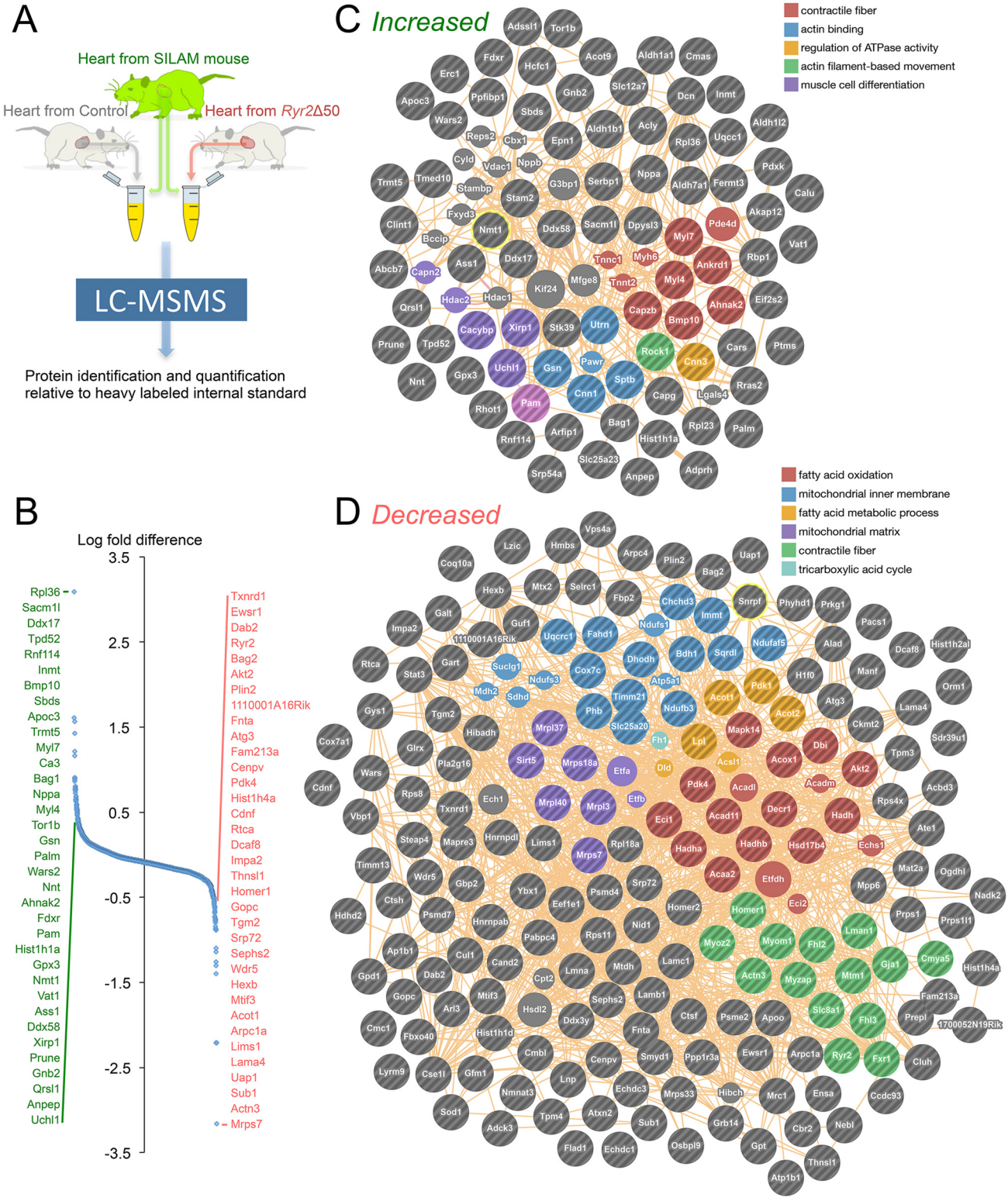

FIGURE 5. **Proteomic analysis of *cRyr2*Δ50 hearts.** *A*, schematic depicting the experimental design of the proteomics experiment, including spike-in with stable isotope-labeled heart tissue (SILAM hearts) to enable quantitative normalization. Four mice per treatment group were pooled and analyzed simultaneously by mass spectroscopy. *B*, distribution of relative protein abundance measurements, with the 25 most enriched proteins (*green*) and 25 most depleted proteins (*red*) between treatment groups listed. *C* and *D*, analysis of up-regulated (*C*) and down-regulated (*D*) proteins identified significantly enriched networks (false discovery rate < 0.05).

Simultaneous cytosolic Ca^{2+} and mitochondrial Ca^{2+} measurements were performed on isolated cardiomyocytes, which were incubated with 5 μM Fura-2-AM (340 and 380 nm excitation; >510 nm emission) and 5 μM Rhod-2-AM (550 nm excitation/580 nm emission) for 15 min and washed for 5 min before imaging using a 10 × 0.5 NA objective Zeiss Axiovert-200M micro-

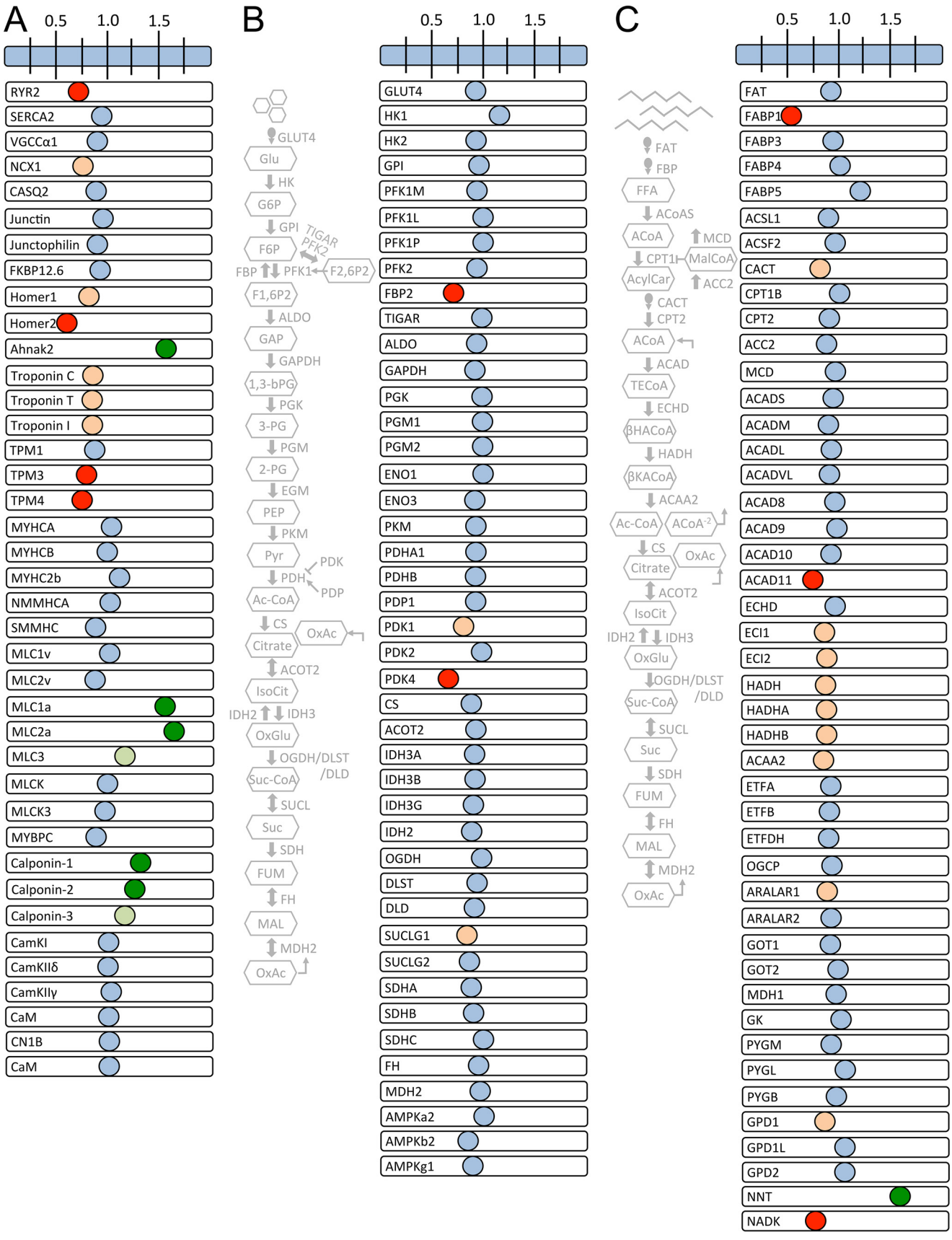
A
0.5
1.0
1.5
RYR2
SERCA2
VGCCα1
NCX1
CASQ2
Junctin
Junctophilin
FKBP12.6
Homer1
Homer2
Ahnak2
Troponin C
Troponin T
Troponin I
TPM1
TPM3
TPM4
MYHCA
MYHCB
MYHC2b
NMMHCA
SMMHC
MLC1v
MLC2v
MLC1a
MLC2a
MLC3
MLCK
MLCK3
MYBPC
Calponin-1
Calponin-2
Calponin-3
CamKI
CamKIIδ
CamKIIγ
CaM
CN1B
CaM
B
0.5
1.0
1.5
GLUT4
Glu
HK
G6P
GPI
F6P
TIGAR
PFK2
FBP
PFK1
F2,6P2
F1,6P2
ALDO
GAP
GAPDH
1,3-bPG
PGK
3-PG
PGM
2-PG
EGM
PEP
PKM
Pyr
PDK
PDH
PDP
Ac-CoA
CS
OxAc
Citrate
ACOT2
IsoCit
IDH2
IDH3
OxGlu
OGDH/DLST
/DLD
Suc-CoA
SUCL
Suc
SDH
FUM
FH
MAL
MDH2
OxAc
GLUT4
HK1
HK2
GPI
PFK1M
PFK1L
PFK1P
PFK2
FBP2
TIGAR
ALDO
GAPDH
PGK
PGM1
PGM2
ENO1
ENO3
PKM
PDHA1
PDHB
PDP1
PDK1
PDK2
PDK4
CS
ACOT2
IDH3A
IDH3B
IDH3G
IDH2
OGDH
DLST
DLD
SUCLG1
SUCLG2
SDHA
SDHB
SDHC
FH
MDH2
AMPKa2
AMPKb2
AMPKg1
C
0.5
1.0
1.5
FAT
FBP
FFA
ACoAS
ACoA
MCD
CPT1
MalCoA
AcylCar
ACC2
CACT
CPT2
ACoA
ACAD
TECoA
ECHD
βHACoA
HADH
βKACoA
ACAA2
Ac-CoA
ACoA-2
CS
Citrate
OxAc
ACOT2
IsoCit
IDH2
IDH3
OxGlu
OGDH/DLST
/DLD
Suc-CoA
SUCL
Suc
SDH
FUM
FH
MAL
MDH2
OxAc
FAT
FABP1
FABP3
FABP4
FABP5
ACSL1
ACSF2
CACT
CPT1B
CPT2
ACC2
MCD
ACADS
ACADM
ACADL
ACADVL
ACAD8
ACAD9
ACAD10
ACAD11
ECHD
ECI1
ECI2
HADH
HADHA
HADHB
ACAA2
ETFA
ETFB
ETFDH
OGCP
ARALAR1
ARALAR2
GOT1
GOT2
MDH1
GK
PYGM
PYGL
PYGB
GPD1
GPD1L
GPD2
NNT
NADK

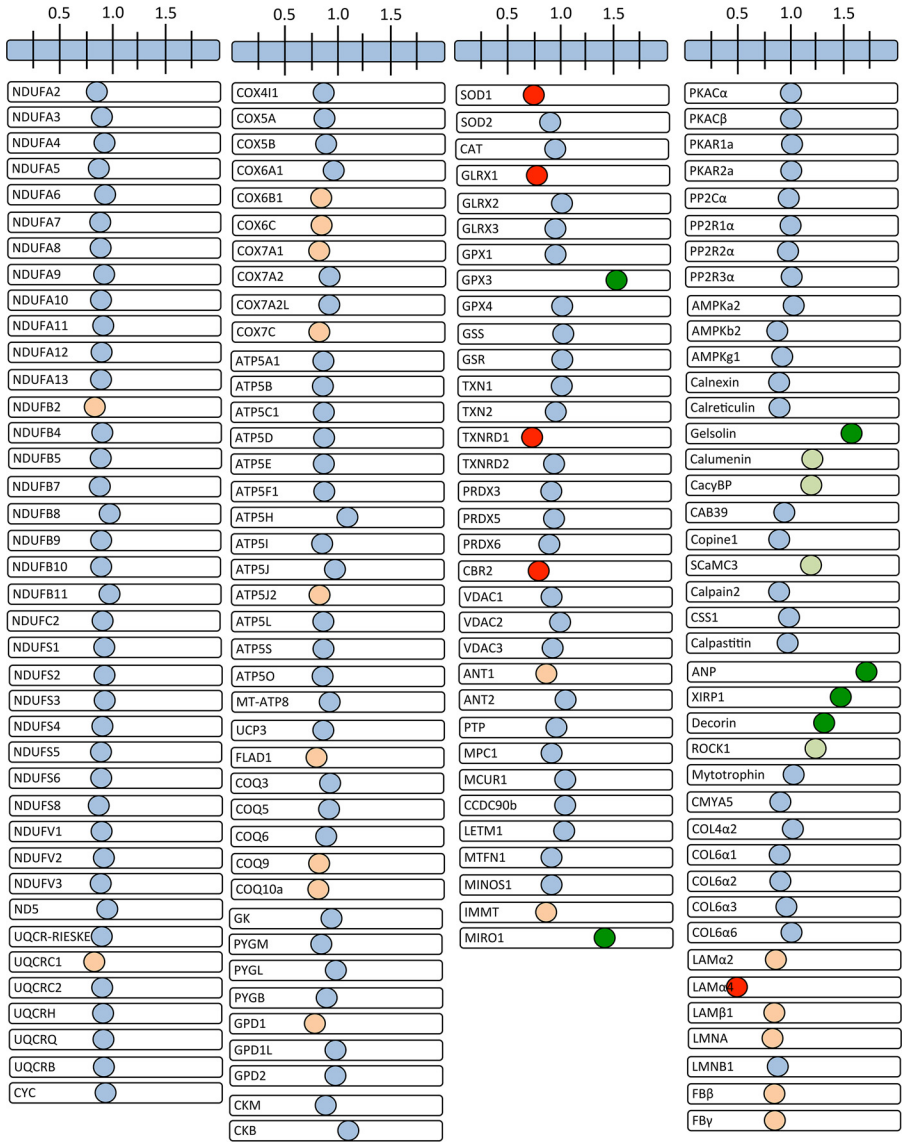

FIGURE 7. **Electron transport chain, ATP synthase complex, and other metabolic effectors in c*Ryr2*Δ50 hearts.** Visualization of the changes of additional cardiac proteins arranged into functional clusters of electron transport chain, metabolic, calcium-sensitive, and cardiac pathology associated proteins is shown. Data are plotted as the -fold difference between c*Ryr2*Δ50 and control hearts (one sample per group made with four pooled hearts per sample to reduce variation). *Red* represents a ≤0.75-fold change, *orange* represents a ≤0.85 change, *pale green* represents a ≥1.15-fold enrichment, and *dark green* represents a ≥1.25-fold enrichment.

scope with a CoolSnapHQ2 CCD Camera (Intelligent Imaging Innovations). Additionally, imaged cells were provided a field stimulation of 80 mA, 5-ms pulses with a hybrid system using a stimulus isolator (World Precision Instruments, Sarasota, CA) and a custom-made programmable stimulator (McAfee Scientific) with periods of: individual analog pulses (to test for responding cells), 0.5-Hz continuous stimulation (to measure Ca^{2+} transients in the context of full cell relaxation), or 6-Hz continuous stimulation (to approximate the rapid stimulation of an *in vivo* heartbeat). This range was also chosen to correlate with the cardiomyocyte function and contractility experiment. Fura-2 ratios to measure relative cytosolic Ca^{2+} and Rhod-2 intensities to measure mitochondrial Ca^{2+} were quantified using the SlideBook software (Intelligent Imaging Innovations). Along with the prior conditions, only cardiomyocytes that displayed stable non-stimulated Fura-2 and Rhod-2 baselines as well as excitability to an initial five field stimulation pulses were considered in this analysis. Cardiomyocytes from at least three independent isolations per treatment group were studied.

Cardiomyocyte function and contractility were assessed as described elsewhere (48). Briefly, a suspension of the isolated ventricular cardiomyocytes was transferred to a chamber with

FIGURE 6. **Parallel analysis of functional protein categories in c*Ryr2*Δ50 hearts.** *A–C*, visualization of the changes of key cardiac proteins arranged into functional clusters of excitation-contraction coupling proteins (*A*), glycolysis and glucose oxidation proteins (*B*), or fat oxidation and other key metabolic proteins (*C*). Data are plotted as the -fold difference between c*Ryr2*Δ50 and control hearts (one sample per group made with four pooled hearts per sample to reduce variation). *Red*, ≤0.75-fold change; *orange*, ≤0.85 change; *pale green*, ≥1.15 enrichment; *dark green*, ≥1.25 enrichment. *Gray schematics* show location of presented glucose and fat oxidation proteins in their respective pathways.

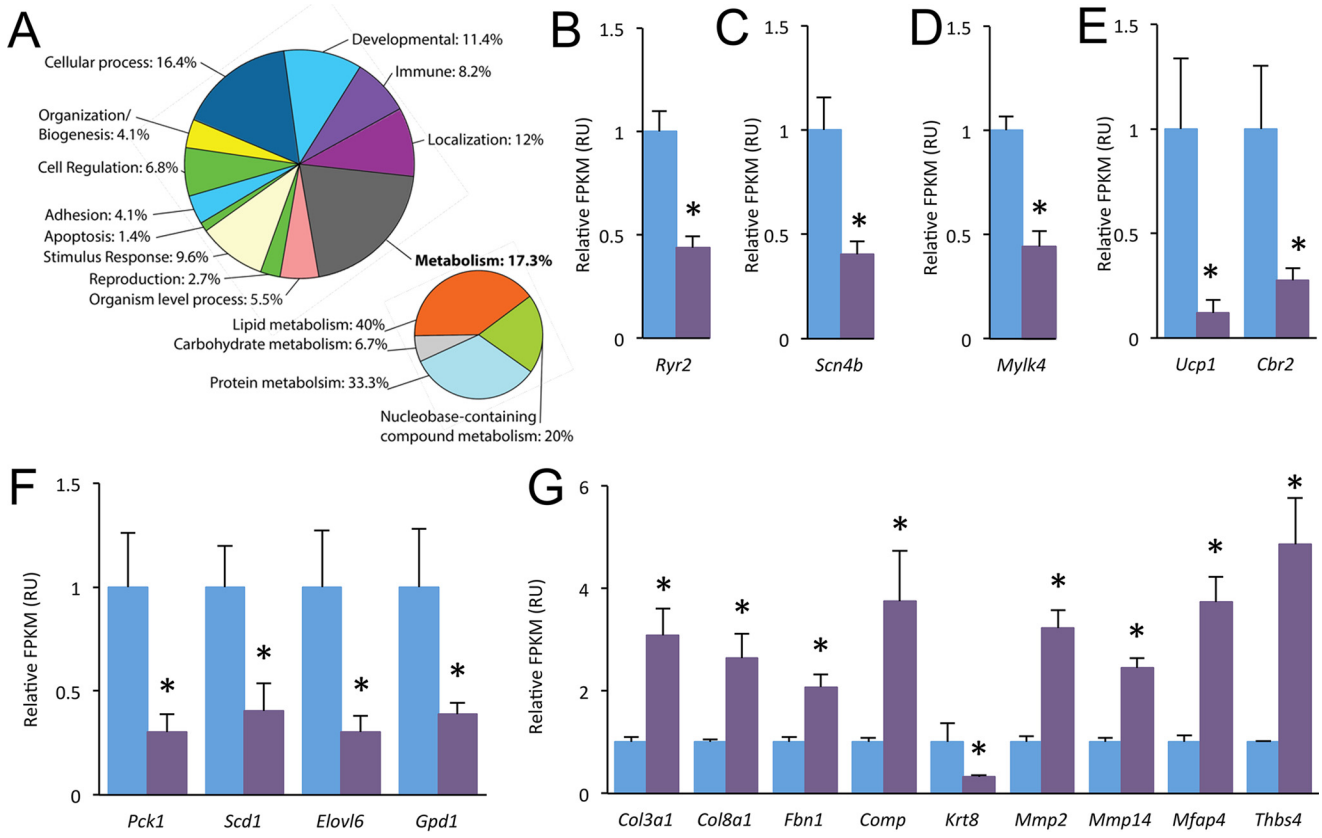

FIGURE 8. **Transcriptomics analysis of *cRyr2*Δ50 hearts.** *A*, biological Gene Ontology (PANTHER) groups of significantly changed genes in the c*Ryr2*Δ50 heart transcriptome. *B–G*, changes in the mRNA levels of *Ryr2* (*B*), as well as other genes involved in excitation-contraction (*C*), contractility (*D*), energetics (*E*), biosynthetic pathways (*F*), and extracellular matrix (*G*) ($n = 4$, *, $p \leq 0.05$). All data were plotted as mean ± S.E. Control = $Ryr2^{flox/wildtype}$ + tamoxifen; c*Ryr2*Δ50: $Ryr2^{flox/wildtype} \times Mhy6\text{-}MerCreMer^{+}$ + tamoxifen.

stimulating electrodes (Cell MicroControls, Norfolk, VA) that was precoated each day with laminin (1 mg/ml) to help immobilize the cells, and then fixed to the heated stage of an Olympus IX70 inverted microscope with 400× quartz optics. The cells were continuously superfused with Tyrode's solution consisting of 1.5 mmol/l $CaCl_2$ in 95% O_2, 5% CO_2 at 0.5–1 ml/min at 34–36 °C. An IonOptix (Milton, MA) video system imaged the cells at 240 Hz, allowing measurement of the degree and rate of myocyte shortening during field stimulation at various frequencies using a programmable stimulator.

In Vivo and ex Vivo Functional Analysis—Cardiac function was examined by echocardiography as described previously (4). Briefly, we utilized a Vevo 770 high-resolution image system (FUJIFILM VisualSonics, Inc., Toronto, Ontario, Canada) (49). Left ventricular mass and systolic function, left ventricular end-systolic and end-diastolic dimensions, interventricular septum thickness, and posterior wall were measured from M-mode traces. Shortening and ejection fraction were calculated as described (49).

Heart rate was assessed by echocardiography and concurrent ECG as described (4). *In vivo* heart rate was also assessed using implantable ETA-F10 ECG radiotelemetry as described (4). Heart rate and rhythmicity were analyzed following recovery from surgery and after the discontinuation of all analgesic drugs.

Ex vivo analyses of heart function and metabolism were carried out using the working heart perfusion model (4, 20, 50). Myocardial substrate utilization was measured in working hearts as detailed elsewhere (20, 51). Glycolysis, as well as myocardial rates of oxidation of palmitate, glucose, and lactate were determined by the quantitative collection of $^{3}H_2O$ or $^{14}CO_2$ produced by hearts perfused with Krebs-Henseleit solution-containing either [9,10-^{3}H]palmitate and [U-^{14}C]lactate or [U-^{14}C]glucose and [5-^{3}H]glucose.

Metabolomics—Mouse hearts were weighed, and then homogenized in 375 μl of 50% MeOH/100 mg of tissue weight with the aid of two 5-mm metal balls shaken for 1 min at 30 Hz. Sample temperature was kept below −10 °C during homogenization. 375 μl of methanol/100 mg of homogenate weight were then added, and the sample was homogenized again for 2 × 1 min. The tube was placed on ice for 30 min and centrifuged at 4 °C and 13,000 rpm for 20 min. The supernatant was collected and stored at −20 °C for UPLC-FTMS and UPLC-MRM/MS. Quantification of carboxylic acids was performed using chemical derivatization with 3-nitrophenylhydrazine followed by subsequent UPLC-MRM/MS determination according to a protocol as described elsewhere (52). Quantitation of glucose, other datable aldoses, and reducing sugar phosphates in the mouse heart tissues was performed using chemical derivatization with anion exchange chromatography followed by UPLC-MRM/MS determination using a previously described protocol (53). Selective quantitation of fructose 1,6-bisphosphate was performed using UPLC-MRM/MS with chemical derivatiza-

tion. AMP, ADP, and ATP levels were assessed using high-performance liquid chromatography in freeze-clamped hearts.

Pdh Activity Assay—Pdh activity was measured in proteins isolated from clamp-frozen, homogenized heart. Buffers included 2 mM EDTA, 2 mM NaF, 1× Complete mini EDTA-free protease inhibitor cocktail tablet per 10 ml of buffer (Roche Applied Science, Basel, Switzerland), and 100 μl of sodium orthovanadate gel to preserve Pdh phosphorylation. Pdh activity and quantity were measured using a Pdh Microplate Assay KIT (Abcam, Cambridge, UK). Pdh activity was normalized to total Pdh in each sample, as well as an internal normalization factor to account for run-to-run variations.

Transcriptomics—RNA was isolated from heart tissue using TRIzol, followed by cleanup (RNeasy; Qiagen, Venlo, The Netherlands). After reverse transcription (SuperScript III; Invitrogen), TaqMan quantitative RT-PCR (qPCR) was conducted using probes from Applied Biosystems (Carlsbad, CA) and PerfeCTa qPCR SuperMix (Quanta Biosciences, Gaithersburg, MD) on a StepOnePlus thermocycler (Applied Biosystems). SYBR Green quantitative RT-PCR was conducted using PerfeCTa SYBR Green qPCR SuperMix (Quanta Biosciences, Gaithersburg MD). Relative gene expression changes were analyzed by the $2^{-\Delta Ct}$ method and plotted in normalized relative units (RU). Hypoxanthine-guanine phosphoribosyltransferase (HPRT) and cyclophilin were used as internal controls, after ensuring that they were not altered in cRyr2KO cardiomyocytes. TaqMan cyclophilin primers were 5′-GTCTGCAAACAGCTCGAA-3′, 5′-ACGCCACTGTCGCTTT-3′, and 5′-/56-FAM/TGCAGCCATGGTCAAC-3′ (produced by Integrated DNA Technologies, Coralville, IA), where FAM is 6-carboxyfluorescein. Additional primer details are available in supplemental Tables S1–S4.

RNA sequencing employed Ion Torrent® technology (Life Technologies). Specifically, total RNA was quantified using the Qubit™ RNA Assay Kit and the Qubit® 2.0 Fluorometer, and its RNA integrity number was measured with the Agilent RNA 6000 Nano Kit on the 2100 Bioanalyzer instrument with the 2100 Expert software. Isolation of mRNA was then performed using the Dynabeads® mRNA DIRECT Micro Kit. Whole transcriptome libraries were constructed using the Ion Total RNA-Seq Kit on the AB Library Builder™ System. Yield and size distribution of the transcriptome libraries were assessed using the Agilent High Sensitivity DNA Kit on the 2100 Bioanalyzer. Templating was constructed using the Ion OneTouch™ 2 System using the Ion PI™ Template OT2 200 Kit V3 before sequencing using the Ion PI™ Sequencing 200 Kit V3 on the Ion Proton™ System. Initial analysis and gene counts were performed on the Torrent Suite™ software (version 4.2.1). Downstream analysis was conducted using the Tuxedo pipeline as well as the CummeRbund software suite in R software (54).

Proteomics—Targeted protein measurement was conducted using Western blots on lysates from mechanically disrupted hearts, which were homogenized and sonicated in ice-cold lysis buffer. Samples were quantified and boiled with loading dye, and 15–50 μg of protein were used in SDS-PAGE electrophoresis. Proteins were then transferred to PVDF membranes using standard semi-dry (≤120 kDa) or wet transfer (>120 kDa) approaches and subsequently treated with targeted primary and horseradish peroxidase-conjugated secondary antibodies. Bands were visualized using an enhanced chemiluminescence detection kit, and then quantified by densitometry. The following commercial antibodies were used: anti-Eea1 (Ab2900, Abcam, Cambridge, UK), anti-Pdh^{S293} (NB110-93429, Novus Biologicals, Littleton, CO), anti-Pdh (Ab110330, Abcam), anti-pAkt^{S473} (9271, Cell Signaling, Danvers, MA), and anti-Akt (2966, Cell Signaling). Rabbit polyclonal anti-RYR2 antibodies were provided by Dr. Anthony Lai. For Ryr2 Western blots, we utilized anti-Eea1 as a large protein loading control, which we previously validated (as described in Ref. 4).

Hearts were briefly perfused to reduce the number of red blood cells and blood-borne proteins, and then rapidly frozen, prior to proteomic analysis. Frozen hearts were mechanically homogenized, and then proteins were isolated and treated as described previously (55). Isolated protein samples from four individual mice per treatment group were then pooled, quantified, and mixed 1:1 by weight with SILAM heart tissue (30) that was prepared in the same manner, before final sample processing as described (55). Sample digestion and offline fractionation were also conducted as described (55) with the exception that endoproteinase LysC was used in place of trypsin for the full digestion. High-pH reverse phase fractionation and mass spectroscopy were conducted as described previously (55). Briefly, each sample was fractionated by high-pH reversed phase on an Agilent Zorbax Extend-C18 analytical column (5 μm, 4.6 × 50 mm) into eight fractions per sample, which were then measured using a Thermo Q-Exactive Hybrid Quadrupole Mass Spectrometer coupled to a Thermo Easy nLC-1000 Liquid Chromatograph. Each fraction was resolved on a 180-min gradient and analyzed on the mass spectrometer in positive ion mode, at 70,000 resolution, from 300 to 20,000 m/z. All mass spectrometry data were captured in profile mode. The 10 most intense peaks were selected (underfill ratio of 10%, 2.2 m/z isolation window, and a normalized collision energy of 28 with 20% stepping) for fragmentation by higher-energy collisional dissociation, and were excluded thereafter for 30 s. Peptides with unassigned charge states, and those with charge 1, were not selected. Peptide identification was carried out using the Andromeda algorithm using the MaxQuant software version 1.5.0.0 from the mouse UniProt database (July 2014), largely using the following settings: endoproteinase LysC cleavage specificity, maximum two missed cleavages, including carbamidomethyl cysteine as a fixed modification and protein N-terminal acetylation, methionine oxidation, and asparagine and glutamine deamination as variable modifications. Match between runs and dependent peptide search were both used in addition to the default 1% false discovery rate settings. Razor peptides were used for quantification, and MaxQuant re-quantification was enabled. Obvious blood-borne, non-cardiac proteins (*e.g.* albumin) were ignored.

Statistical Analysis—Data are expressed as mean ± S.E., unless otherwise indicated. Results were considered statistically significant when $p \leq 0.05$ using Student's t test or, where appropriate, two-factor mixed design analysis of variance with repeated measures and Bonferroni's post test. All experiments were repeated on at least three cRyr2Δ50 mice and at least three

of their tamoxifen-injected littermate controls ($Ryr2^{flox/wildtype}$) unless otherwise specified.

Author Contributions—M. J. B. conceived studies and wrote the manuscript. M. J. B., R. W., H. C., P. A., R. F. A., J. H., D. M., and M. P. designed and performed experiments and analyzed data. R. W., H. C., P. A., R. F. A., J. H., D. M., M. P., N. E. S., L. B., J. E. K., S. R. W. C., D. F., R. W. B., C. H. B., L. J. F., T. M., and M. F. A. reviewed the manuscript. N. E. S. designed and performed experiments. L. B. and J. E. K. performed experiments and analyzed data. S. R. W. C. and D. F. provided access to essential resources. R. W. B., C. H. B., L. J. F., T. M., and E. D. W. M. designed studies and provided access to essential resources. M. F. A. conceived studies, designed studies, and provided access to essential resources. J. D. J. conceived studies, analyzed data, co-wrote/edited the manuscript, and is the ultimate guarantor of this work.

Acknowledgments—We thank Nikolay Stoynov for assistance with mass spectrometry. We thank Dr. A. Lai for the Ryr2 antibody. We thank Dr. Carles Vilariño-Güell and Daniel Bong for access to RNA-seq resources. Mass spectrometry infrastructure used here was supported by the Canada Foundation for Innovation and the British Columbia Knowledge Development Fund.

References

1. Lanner, J. T., Georgiou, D. K., Joshi, A. D., and Hamilton, S. L. (2010) Ryanodine receptors: structure, expression, molecular details, and function in calcium release. *Cold Spring Harb. Perspect. Biol.* **2,** a003996
2. Monfredi, O., Maltsev, V. A., and Lakatta, E. G. (2013) Modern concepts concerning the origin of the heartbeat. *Physiology* **28,** 74–92
3. George, C. H., Jundi, H., Thomas, N. L., Fry, D. L., and Lai, F. A. (2007) Ryanodine receptors and ventricular arrhythmias: emerging trends in mutations, mechanisms and therapies. *J. Mol. Cell. Cardiol.* **42,** 34–50
4. Bround, M. J., Asghari, P., Wambolt, R. B., Bohunek, L., Smits, C., Philit, M., Kieffer, T. J., Lakatta, E. G., Boheler, K. R., Moore, E. D. W., Allard, M. F., and Johnson, J. D. (2012) Cardiac ryanodine receptors control heart rate and rhythmicity in adult mice. *Cardiovasc. Res.* **96,** 372–380
5. Yang, H. T., Tweedie, D., Wang, S., Guia, A., Vinogradova, T., Bogdanov, K., Allen, P. D., Stern, M. D., Lakatta, E. G., and Boheler, K. R. (2002) The ryanodine receptor modulates the spontaneous beating rate of cardiomyocytes during development. *Proc. Natl. Acad. Sci. U.S.A.* **99,** 9225–9230
6. Wilkins, B. J., and Molkentin, J. D. (2004) Calcium-calcineurin signaling in the regulation of cardiac hypertrophy. *Biochem. Biophys. Res. Commun.* **322,** 1178–1191
7. Zou, Y., Liang, Y., Gong, H., Zhou, N., Ma, H., Guan, A., Sun, A., Wang, P., Niu, Y., Jiang, H., Takano, H., Toko, H., Yao, A., Takeshima, H., Akazawa, H., *et al.* (2011) Ryanodine receptor type 2 is required for the development of pressure overload-induced cardiac hypertrophy. *Hypertension* **58,** 1099–1110
8. Scriven, D. R. L., Asghari, P., and Moore, E. D. W. (2013) Microarchitecture of the dyad. *Cardiovasc. Res.* **98,** 169–176
9. Crossman, D. J., Ruygrok, P. N., Ruygrok, P. R., Soeller, C., and Cannell, M. B. (2011) Changes in the organization of excitation-contraction coupling structures in failing human heart. *PLoS ONE* **6,** e17901
10. Kandilci, H. B., Tuncay, E., Zeydanli, E. N., Sozmen, N. N., and Turan, B. (2011) Age-related regulation of excitation-contraction coupling in rat heart. *J. Physiol. Biochem.* **67,** 317–330
11. Bidasee, K. R., Dinçer Ü. D, and Besch, H. R., Jr. (2001) Ryanodine receptor dysfunction in hearts of streptozotocin-induced diabetic rats. *Mol. Pharmacol.* **60,** 1356–1364
12. Matsui, H., MacLennan, D. H., Alpert, N. R., and Periasamy, M. (1995) Sarcoplasmic reticulum gene expression in pressure overload-induced cardiac hypertrophy in rabbit. *Am. J. Physiol. Cell Physiol.* **268,** C252–C258
13. Milnes, J. T., and MacLeod, K. T. (2001) Reduced ryanodine receptor to dihydropyridine receptor ratio may underlie slowed contraction in a rabbit model of left ventricular cardiac hypertrophy. *J. Mol. Cell. Cardiol.* **33,** 473–485
14. Stanley, W. C., Recchia, F. A., and Lopaschuk, G. D. (2005) Myocardial substrate metabolism in the normal and failing heart. *Physiol. Rev.* **85,** 1093–1129
15. Doenst, T., Nguyen, T. D., and Abel, E. D. (2013) Cardiac metabolism in heart failure: implications beyond ATP production. *Circ. Res.* **113,** 709–724
16. Rizzuto, R., and Pozzan, T. (2006) Microdomains of intracellular Ca^{2+}: molecular determinants and functional consequences. *Physiol. Rev.* **86,** 369–408
17. Denton, R. M. (2009) Regulation of mitochondrial dehydrogenases by calcium ions. *Biochim. Biophys. Acta.* **1787,** 1309–1316
18. Glancy, B., Willis, W. T., Chess, D. J., and Balaban, R. S. (2013) Effect of calcium on the oxidative phosphorylation cascade in skeletal muscle mitochondria. *Biochemistry* **52,** 2793–2809
19. Glancy, B., and Balaban, R. S. (2012) Role of mitochondrial Ca^{2+} in the regulation of cellular energetics. *Biochemistry* **51,** 2959–2973
20. Bround, M. J., Wambolt, R., Luciani, D. S., Kulpa, J. E., Rodrigues, B., Brownsey, R. W., Allard, M. F., and Johnson, J. D. (2013) Cardiomyocyte ATP production, metabolic flexibility, and survival require calcium flux through cardiac ryanodine receptors *in vivo*. *J. Biol. Chem.* **288,** 18975–18986
21. Chen, Y., Csordás, G., Jowdy, C., Schneider, T. G., Csordás, N., Wang, W., Liu, Y., Kohlhaas, M., Meiser, M., Bergem, S., Nerbonne, J. M., Dorn, G. W., 2nd, and Maack, C. (2012) Mitofusin 2-containing mitochondrial-reticular microdomains direct rapid cardiomyocyte bioenergetic responses via interorganelle Ca^{2+} crosstalk. *Circ. Res.* **111,** 863–875
22. Liu, T., and O'Rourke, B. (2008) Enhancing mitochondrial Ca^{2+} uptake in myocytes from failing hearts restores energy supply and demand matching. *Circ. Res.* **103,** 279–288
23. Pan, X., Liu, J., Nguyen, T., Liu, C., Sun, J., Teng, Y., Fergusson, M. M., Rovira, I. I., Allen, M., Springer, D. A., Aponte, A. M., Gucek, M., Balaban, R. S., Murphy, E., and Finkel, T. (2013) The physiological role of mitochondrial calcium revealed by mice lacking the mitochondrial calcium uniporter. *Nat. Cell Biol.* **15,** 1464–1472
24. Gong, G., Liu, X., and Wang, W. (2014) Regulation of metabolism in individual mitochondria during excitation-contraction coupling. *J. Mol. Cell. Cardiol.* **76,** 235–246
25. Luongo, T. S., Lambert, J. P., Yuan, A., Zhang, X., Gross, P., Song, J., Shanmughapriya, S., Gao, E., Jain, M., Houser, S. R., Koch, W. J., Cheung, J. Y., Madesh, M., and Elrod, J. W. (2015) The mitochondrial calcium uniporter matches energetic supply with cardiac workload during stress and modulates permeability transition. *Cell Rep.* **12,** 23–34
26. Kwong, J. Q., Lu, X., Correll, R. N., Schwanekamp, J. A., Vagnozzi, R. J., Sargent, M. A., York, A. J., Zhang, J., Bers, D. M., and Molkentin, J. D. (2015) The mitochondrial calcium uniporter selectively matches metabolic output to acute contractile stress in the heart. *Cell Rep.* **12,** 15–22
27. Wu, Y., Rasmussen, T. P., Koval, O. M., Joiner, M.-L. A., Hall, D. D., Chen, B., Luczak, E. D., Wang, Q., Rokita, A. G., Wehrens, X. H. T., Song, L.-S., and Anderson, M. E. (2015) The mitochondrial uniporter controls fight or flight heart rate increases. *Nat. Commun.* **6,** 6081
28. Hiess, F., Vallmitjana, A., Wang, R., Cheng, H., ter Keurs, H. E. D. J., Chen, J, Hove-Madsen, L., Benitez, R., and Chen, S. R. W. (2015) Distribution and function of cardiac ryanodine receptor clusters in live ventricular myocytes. *J. Biol. Chem.* **290,** 20477–20487
29. Patel, M. S., Nemeria, N. S., Furey, W., and Jordan, F. (2014) The pyruvate dehydrogenase complexes: structure-based function and regulation. *J. Biol. Chem.* **289,** 16615–16623
30. Zanivan, S., Krueger, M., and Mann, M. (2012) *In vivo* quantitative proteomics: the SILAC mouse. *Methods Mol. Biol.* **757,** 435–450
31. Song, W., Wang, H., and Wu, Q. (2015) Atrial natriuretic peptide in cardiovascular biology and disease (*NPPA*). *Gene* **569,** 1–6
32. Komuro, A., Masuda, Y., Kobayashi, K., Babbitt, R., Gunel, M., Flavell, R. A., and Marchesi, V. T. (2004) The AHNAKs are a class of giant pro-

peller-like proteins that associate with calcium channel proteins of cardiomyocytes and other cells. *Proc. Natl. Acad. Sci. U.S.A.* **101,** 4053–4058
33. Pouliquin, P., Pace, S. M., and Dulhunty, A. F. (2009) *In vitro* modulation of the cardiac ryanodine receptor activity by Homer1. *Pflugers Arch.* **458,** 723–732
34. Hernandez, O. M., Jones, M., Guzman, G., and Szczesna-Cordary, D. (2007) Myosin essential light chain in health and disease. *Am. J. Physiol. Heart Circ. Physiol.* **292,** H1643–H1654
35. Lu, D., Zhang, L., Bao, D., Lu, Y., Zhang, X., Liu, N., Ge, W., Gao, X., Li, H., and Zhang, L. (2014) Calponin1 inhibits dilated cardiomyopathy development in mice through the ϵPKC pathway. *Int. J. Cardiol.* **173,** 146–153
36. Mor, I., Cheung, E. C., and Vousden, K. H. (2011) Control of glycolysis through regulation of PFK1: old friends and recent additions. *Cold Spring Harb. Symp. Quant. Biol.* **76,** 211–216
37. Sheeran, F. L., Rydström, J., Shakhparonov, M. I., Pestov, N. B., and Pepe, S. (2010) Diminished NADPH transhydrogenase activity and mitochondrial redox regulation in human failing myocardium. *Biochim. Biophys. Acta* **1797,** 1138–1148
38. Herrer, I., Roselló-Lletí, E., Rivera, M., Molina-Navarro, M. M., Tarazón, E., Ortega, A., Martínez-Dolz, L., Triviño, J. C., Lago, F., González-Juanatey, J. R., Bertomeu, V., Montero, J. A., and Portolés, M. (2014) RNA-sequencing analysis reveals new alterations in cardiomyocyte cytoskeletal genes in patients with heart failure. *Lab. Invest.* **94,** 645–653
39. Hoerter, J., Gonzalez-Barroso, M.-D.-M., Couplan, E., Mateo, P., Gelly, C., Cassard-Doulcier, A.-M., Diolez, P., and Bouillaud, F. (2004) Mitochondrial uncoupling protein 1 expressed in the heart of transgenic mice protects against ischemic-reperfusion damage. *Circulation* **110,** 528–533
40. de Haas, H. J., Arbustini, E., Fuster, V., Kramer, C. M., and Narula, J. (2014) Molecular imaging of the cardiac extracellular matrix. *Circ. Res.* **114,** 903–915
41. Jeong, J. Y., Jeoung, N. H., Park, K.-G., and Lee, I.-K. (2012) Transcriptional regulation of pyruvate dehydrogenase kinase. *Diabetes Metab J.* **36,** 328–335
42. Sun, W., Liu, Q., Leng, J., Zheng, Y., and Li, J. (2015) The role of Pyruvate Dehydrogenase Complex in cardiovascular diseases. *Life Sci.* **121,** 97–103
43. García-Pérez, C., Schneider, T. G., Hajnóczky, G., and Csordás, G. (2011) Alignment of sarcoplasmic reticulum-mitochondrial junctions with mitochondrial contact points. *Am. J. Physiol. Heart Circ. Physiol.* **301,** H1907–H1915
44. Min, C. K., Yeom, D. R., Lee, K. E., Kwon, H. K., Kang, M., Kim, Y. S., Park, Z. Y., Jeon, H., and Kim, D. H. (2012) Coupling of ryanodine receptor 2 and voltage-dependent anion channel 2 is essential for Ca^{2+} transfer from the sarcoplasmic reticulum to the mitochondria in the heart. *Biochem. J.* **447,** 371–379
45. Koitabashi, N., Bedja, D., Zaiman, A. L., Pinto, Y. M., Zhang, M., Gabrielson, K. L., Takimoto, E., and Kass, D. A. (2009) Avoidance of transient cardiomyopathy in cardiomyocyte-targeted tamoxifen-induced MerCreMer gene deletion models. *Circ. Res.* **105,** 12–15
46. Fernando, V. (2006) *Cardiovascular Proteomics: Methods and Protocols*, Humana Press, NJ, 10.1385/1597452149
47. Picht, E., Zima, A. V., Blatter, L. A., and Bers, D. M. (2007) SparkMaster: automated calcium spark analysis with ImageJ. *Am. J. Physiol. Cell Physiol.* **293,** C1073–C1081
48. Williams, S., Pourrier, M., McAfee, D., Lin, S., and Fedida, D. (2014) Ranolazine improves diastolic function in spontaneously hypertensive rats. *Am. J. Physiol. Heart Circ. Physiol.* **306,** H867–H881
49. Gomez, A. M., and Richard, S. (2004) Mutant cardiac ryanodine receptors and ventricular arrhythmias: is "gain-of-function" obligatory? *Cardiovasc. Res.* **64,** 3–5
50. Allard, M. F., Parsons, H. L., Saeedi, R., Wambolt, R. B., and Brownsey, R. (2007) AMPK and metabolic adaptation by the heart to pressure overload. *Am. J. Physiol. Heart Circ. Physiol.* **292,** H140–H148
51. Allard, M. F., Schönekess, B. O., Henning, S. L., English, D. R., and Lopaschuk, G. D. (1994) Contribution of oxidative metabolism and glycolysis to ATP production in hypertrophied hearts. *Am. J. Physiol.* **267,** H742–H750
52. Han, J., Gagnon, S., Eckle, T., and Borchers, C. H. (2013) Metabolomic analysis of key central carbon metabolism carboxylic acids as their 3-nitrophenylhydrazones by UPLC/ESI-MS. *Electrophoresis* **34,** 2891–2900
53. Han, J., Tschernutter, V., Yang, J., Eckle, T., and Borchers, C. H. (2013) Analysis of selected sugars and sugar phosphates in mouse heart tissue by reductive amination and liquid chromatography-electrospray ionization mass spectrometry. *Anal. Chem.* **85,** 5965–5973
54. Trapnell, C., Roberts, A., Goff, L., Pertea, G., Kim, D., Kelley, D. R., Pimentel, H., Salzberg, S. L., Rinn, J. L., and Pachter, L. (2012) Differential gene and transcript expression analysis of RNA-seq experiments with TopHat and Cufflinks. *Nat. Protoc.* **7,** 562–578
55. Albu, R. F., Chan, G. T., Zhu, M., Wong, E. T. C., Taghizadeh, F., Hu, X., Mehran, A. E., Johnson, J. D., Gsponer, J., and Mayor, T. (2015) A feature analysis of lower solubility proteins in three eukaryotic systems. *J. Proteomics* **118,** 21–38